Shape-Selective Synthesis of Intermetallic Pd_3Pb Nanocrystals and Enhanced Catalytic Properties in the Direct Synthesis of Hydrogen Peroxide

Vanitha Reddy Naina,[⊥] Sheng Wang,[⊥] Dmitry I. Sharapa, Michael Zimmermann, Martin Hähsler, Lukas Niebl-Eibenstein, Junjun Wang, Christof Wöll, Yuemin Wang, Sanjay Kumar Singh, Felix Studt, and Silke Behrens*

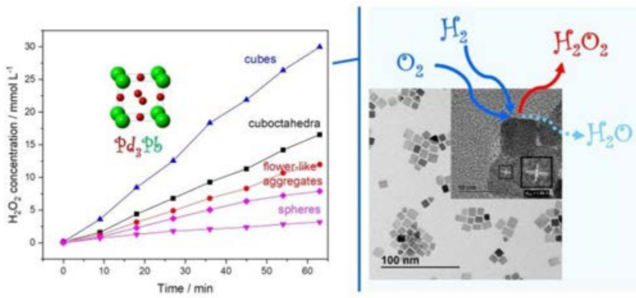

ABSTRACT: Hydrogen peroxide production by direct synthesis ($H_2 + O_2 \rightarrow H_2O_2$) is a promising alternative to the commercialized indirect process involving sequential hydrogenation and oxidation of anthraquinones. Metal dopants are known to enhance the performance of Pd based catalysts in this reaction by increasing H_2O_2 rates and selectivity. Recently, binary and ternary Pd based alloys with Pb have been proposed as catalysts by theoretical studies, but these compositions lack experimental proof. Herein, shape selective Pd_3Pb nanocrystals were created to produce catalysts where the active and doping metal are colocalized to a fine extent. This strategy enables us to study the effects of both Pb doping and nanocrystal shape on the catalytic performance in direct H_2O_2 synthesis. In order to achieve these goals, we developed a procedure for the shape controlled synthesis of Pb doped nanocrystals with phase pure, intermetallic Pd_3Pb composition. By a change of the ligands, uniform Pd_3Pb nanocrystals with cubic, cuboctahedral, and spherical shapes as well as flowerlike aggregates were obtained, which were supported on acid treated TiO_2. We show that the catalytic efficiency in direct H_2O_2 synthesis not only is influenced by the nanocrystal composition but also depends on the particle shape. Pd_3Pb cubes, predominately terminated by their (200) facets, outperformed not only the monometallic Pd reference catalyst but also Pd_3Pb nanocrystals with other shapes. Further DFT calculations and surface studies indicated not only the electronic modification of Pd surface atoms with a higher barrier for O_2 dissociation on Pd_3Pb but also a lack of larger Pd ensembles in Pd_3Pb cubes which are known to cleave O−O bonds and form water.

KEYWORDS: *catalysis, hydrogen peroxide, intermetallic nanocrystals, palladium, lead, infrared spectroscopy, DFT calculations*

INTRODUCTION

Hydrogen peroxide (H_2O_2) is an increasingly important base chemical with high oxidation potential and low environmental impact, as water is the only byproduct in many of its applications.[1,2] H_2O_2 is used, for example, in the pulp and paper industry, in wastewater treatment, as a disinfectant, and as a selective oxidant in chemical manufacture and moves an industry of almost 4 billion dollars, projected to reach 6 billion dollars by 2023.[3] Currently, the vast majority of the chemical is produced through the indirect Riedl−Pfleiderer process, which involves the sequential hydrogenation and oxidation of anthraquinones in an organic working solution.[1,4] The Riedl−Pfleiderer process involves significant capital expenditures and operating costs, which has motivated industry and academia to develop alternative processes for H_2O_2 synthesis, in particular its direct synthesis from oxygen and hydrogen and electrochemical processes, which share similar attributes in terms of the catalysis.[5] Electrochemical H_2O_2 production proceeds via the cathodic two electron reduction of O_2 with noble metals and their alloys[3,6−10] or metal free, carbon based materials as electrocatalysts.[11−13] Recently, the direct electrosynthesis of a pure aqueous H_2O_2 solution (up to 20 wt %) was achieved in combination with a solid electrolyte.[14] The photocatalytic production of H_2O_2 from O_2 and H_2O using solar energy is also highly attractive, but the low photocatalytic efficiency is still a major challenge.[15,16]

The direct synthesis of H_2O_2 from H_2 and O_2 is a promising atom efficient alternative with clear benefits over the Riedl−Pfleiderer process, as the infrastructure is simplified, less energy is consumed, green solvents (water or alcohols) are used, organic substrates are missing, and it may be reasonably scaled to small facilities for on site use.[17] Although the first patent for H_2O_2 manufacture from H_2 and O_2 was published in 1914, its full industrial implementation has been hampered, primarily due to poor H_2O_2 selectivity and stability of the Pd based catalysts.[4,18,19] Since then, the direct H_2O_2 synthesis has attracted great interest in academia and industry as such or in tandem with selective oxidation reactions (e.g., in the hydrogen peroxide to propylene oxide (HPPO) process[17] or in chemoenzymatic oxidation cascades).[20] To date, most studies have been based on supported Pd nanocrystals (NCs), which have remained the most active catalysts.[21−23] However, Pd particles are also highly active for H_2O_2 degradation reactions and therefore exhibit poor selectivity. To increase the H_2O_2 selectivity, the complete scission of the O−O bond needs to be avoided by decreasing the extent of electron back donation to the $2\pi^*$ orbitals of O_2, and the H_2O_2 formed needs to be stabilized.[17] Acid (e.g., H_2SO_4) and/or halide (e.g., Cl^-, Br^-) promoters improve H_2O_2 selectivity by stabilizing HOO^- species and blocking sites for side reactions.[24−26] Liquid phase promoters, however, may lead to reactor corrosion and leaching of the active metal particles, and their effect on reactions that utilize H_2O_2 downstream is not well understood. Hence, designing novel catalysts with improved H_2O_2 selectivity and productivity in the absence of these promoters is highly desirable but is also a major challenge. Various material properties influence the overall performance of Pd catalysts in this reaction, including the particle size[27] and morphology,[28−30] surface adsorbates,[31] and the nature of the support.[32−34] Electronic effects and site modification/isolation through addition of metal dopants comprise an effective strategy to enhance the selectivity of Pd catalysts. Pd and Pt particles alloyed with noble metals (e.g., Au,[35] Ag[36]) or base metals (e.g., Ga,[37,38] In,[37,38] Sn,[38,39] Sb,[40] Te[41]) were shown to produce H_2O_2 with high efficiency. High H_2O_2 selectivity has been achieved for Au or Sn doped Pd catalysts in the absence of acid and halide promoters, demonstrating that the sites for H_2O_2 synthesis and H_2O_2 degradation are different and can be isolated.[38,39,42−44] Au was suggested not only to rehybridize orbitals within the surface but also to withdraw electrons from Pd atoms, reducing electron back donation. Au was further suggested to change the geometrical surface structure, reducing the prevalence of multiple Pd sites[6] and, thus, the distribution of active sites among those that preferentially form H_2O_2 (single Pd sites) and those that preferentially form H_2O (groupings of multiple Pd atoms).[45] Even C supported $PdCl_x$ single site species were recently shown to reduce H_2O_2 degradation.[46] For metal NCs, facet dependent catalytic properties were further observed in direct H_2O_2 syn thesis.[28,30,36,47] Overall, the enhanced catalytic properties of multimetallic catalysts have been attributed to a complex set of various factors, including synergistic effects, modified elec tronic and/or geometrical structures of the active surface sites, and the formation of metal oxide surface species (M_xO_y) or lattice hydrogen (PdH_x).[48] However, the sites that can selectively produce H_2O_2 have not been identified and the role of the additives remains unclear. On the other hand, theoretical studies have been carried out in a search for novel catalyst compositions. On the basis of DFT calculations, Au Ag and Pt Ga alloys, intermetallic compounds, and ternary alloys of Au, Ag, and Pd were predicted to be H_2O_2 catalysts with improved catalytic performance.[49] In a recent computational chemistry study, the average number of valence electrons of Pd shell atoms was identified as an intrinsic factor for the activity and selectivity of the Pd based nanocatalysts, which can be effectively tuned by the electronegativity of additional metal dopants. Dopants with suitable electronegativity (in particular an electronegativity higher than that of Pd) were suggested to withdraw electrons from Pd shell atoms and thereby decrease the extent of electron back donation.[50] In particular, Pb or W were proposed as dopants in binary, Pd based alloy catalysts, maximizing activity and selectivity for H_2O_2 at the same time. Indeed, Pb is also well known to modify the Pd sites in Lindlar catalysts which hinder the formation of Pd hydride in the proximity of the catalyst surface and avoid overhydrogenation to undesired alkanes in the catalytic partial hydrogenation of alkynes to alkenes.[51] The reduced Lindlar catalyst is composed of either a Pd Pb alloy or a Pd_3Pb intermetallic compound, below which remained the essentially unchanged Pd. To the best of our knowledge, up to now, no experimental evidence has been provided for the promotional effects of Pb doping in Pd catalysts for direct H_2O_2 synthesis.

This shows that the H_2O_2 selectivity and productivity of Pd based NCs is determined by a complex set of factors that needs to be considered and addressed in their synthesis. Herein, we show a facile route to create a series of unique intermetallic Pd_3Pb NCs. The successful creation of intermetallic Pd_3Pb NCs with well defined size, structure, composition, and shape provides an ideal platform to study the promotional effects of Pb doping on Pd catalysts, especially the surface geometry and composition, on direct H_2O_2 synthesis. For catalytic tests, the NCs were successively immobilized on an acid treated TiO_2 support. Acid pretreatment was previously demonstrated to further enhance catalytic selectivity in direct H_2O_2 syn thesis.[33,52] For the first time, we report here on the catalytic performance of these shape selective, intermetallic Pd_3Pb catalysts in direct H_2O_2 synthesis. In particular, Pd_3Pb NCs with a cubic shape reveal an outstanding H_2O_2 productivity because of their ordered structure, well defined morphology, and alloy effect.

EXPERIMENTAL SECTION

Nanocrystal Synthesis. All syntheses were performed using standard Schlenk techniques under an argon atmosphere.

Pd_3Pb Cubes. $Pd(acac)_2$ (0.675 mmol; 205.82 mg) and $Pb(acac)_2$ (0.225 mmol, 91.22 mg) were dissolved in a solution of oleyl amine (OLAM) (18.2 mmol, 6 mL), oleic acid (OLAC) (8.8 mmol, 2.8 mL), and dioctyl ether (30 mL). While it was stirred with a magnetic Teflon stirrer, the reaction mixture was heated to 60 °C, which was maintained for 30 min. Trioctylphosphine (TOP; 4.4 mmol, 2 mL) was added dropwise to yield a pale yellow solution. The reaction mixture was then further heated to 200 °C (heating rate 10 °C/min) and was kept at that temperature for another 40 min. The solution turned black, indicating NC formation. The reaction mixture was cooled to room temperature, and the NCs were collected in four centrifuge tubes (50 mL each). The volume was filled up to 45 mL with acetone, and the NCs were precipitated by centrifugation. The NCs were purified by successively dispersing and precipitating the NCs with chloroform and acetone, respectively. The NCs were collected as a colloidal dispersion in $CHCl_3$.

Pd_3Pb Flowerlike Aggregates. A procedure similar to that for Pd_3Pb nanocubes. However, L ascorbic acid (2 mmol, 352.24 mg) was added instead of TOP to the original solution of Pd(acac)$_2$ (0.675 mmol, 205.82 mg), Pb(acac)$_2$ (0.225 mmol, 91.22 mg), OLAM (18.2 mmol, 6 mL), and OLAC (8.0 mmol, 2.8 mL) in dioctyl ether (30 mL). The solution was stirred for 30 min at 60 °C, and then the reaction temperature was increased to 140 °C (heating rate 10 °C/min), which was maintained for 40 min. After the solution was cooled to room temperature, the flowerlike Pd_3Pb aggregates were purified and dispersed in $CHCl_3$ (see above).

Pd_3Pb Cuboctahedra. A procedure similar to that for Pd_3Pb nanocubes was followed, except TOP was not added to the reaction mixture containing Pd(acac)$_2$ (0.675 mmol, 205.82 mg), Pb(acac)$_2$ (0.225 mmol, 91.22 mg), OLAM (18.2 mmol, 6 mL), and OLAC (8.8 mmol, 2.8 mL) in dioctyl ether (30 mL). The reaction mixture was heated to 60 °C. After 30 min of heating, the temperature was raised to 200 °C (heating rate 10 °C/min) and that temperatue was maintained for another 40 min. Due to the fact that TOP was not added, the solution turned black at around 160 °C. The reaction mixture was cooled to room temperature, and the NCs were purified and dispersed in $CHCl_3$ (see above).

Pd_3Pb Spheres. Pd(acac)$_2$ (0.675 mmol, 205.82 mg) and Pb(acac)$_2$ (0.225 mmol, 91.22 mg) (Pd/Pb precursor ratio 3/1; total amount of metal precursors 0.9 mmol) were dissolved in 30 mL of dioctyl ether, OLAM (18.2 mmol, 6 mL), and OLAC (8.8 mmol, 2.8 mL). The reaction mixture was heated to 60 °C, and that tempreature was maintained for 30 min. After dropwise addtion of TOP (2.2 mmol, 1 mL), the reaction mixture was heated to 170 °C (heating rate of 10 °C/min). As soon as the reaction temperature reached 170 °C, it was decreased again to 160 °C (to control the growth of NCs) and the mixture was stirred for 40 min. After the mixture was cooled to room temperature, the spherical Pd_3Pb NCs were purified and dispersed in $CHCl_3$ (see above).

Preparation of Catalysts. TiO_2 (10 g) was pretreated with H_2SO_4 (2 wt %, 100 mL) for 3 h at room temperature with stirring. The support material was filtered and washed with H_2SO_4 (2 wt %). The support was dried overnight under vacuum and collected after grinding to a powder. To prepare the catalysts (5 wt % total metal loading), metal NCs were adsorbed on the pretreated support (s TiO_2) from the colloidal dispersion by adding s TiO_2 to the appropriate amount of NCs in chloroform and stirring for 3 h. The catalyst was treated with ultrasound (2 min) to achieve a homogeneous NC distribution over the support material. The catalysts were recovered by centrifugation and washed with ethanol. The catalysts were dried overnight under vacuum at 30 °C and collected as gray powders after grinding.

Characterization. The NCs were characterized by trans mission electron microscopy (TEM) using a FEI Tecnai F20 ST TEM (operating voltage 200 kV) with a field emission gun and an EDAX EDS X ray spectrometer (Si (Li) detecting unit, super ultrathin window, active area 30 mm^2, resolution 135 eV at 5.9 keV). For scanning electron microscopy (SEM), a Zeiss GeminiSEM500 instrument was employed, which was equipped with a Schottky type thermal field emission cathode. A small droplet of the NC dispersion or the catalyst powder, accordingly, was deposited on amorphous carbon coated, 400 mesh Cu grids and air dried. On the basis of the TEM images, the mean particle diameter was calculated by measuring the size of typically at least 100 particles. Powder X ray diffraction (XRD) patterns were recorded on a PANalytical X'Pert Pro X ray diffractometer employing a Bragg−Brentano geometry with Cu Kα radiation and a Ni filter. The range between 5 and 120° was measured over 16 h. The reflections were compared to reference data reported in the International Centre for Diffraction Data (ICDD) database. The crystallite sizes of the NCs was determined according to the Scherrer equation to be 50.6, 55.9, and 65.5° (2θ) and averaged. For the small spherical NCs, only the reflection at 65.8° (2θ) was considered. The Pd and Pb contents of the NCs were determined for the dried NC powder and the supported catalysts by inductively coupled plasma optical emission spectroscopy (ICP OES, Agilent 725 ICP OES spectrometer). For ICP OES analysis, the NCs and the supported catalysts were dissolved in aqua regia and HF/aqua regia (HF/aqua regia volume ratio 2/1), respectively. Infrared spectroscopy investigations were conducted with a dedicated ultrahigh vacuum (UHV) apparatus described elsewhere.[53] Briefly, it combines a state of the art infrared spectrometer (Bruker Vertex 80v) and a multichamber UHV system (Prevac). The TiO_2 supported pure Pd and Pd_3Pb NCs were first pressed into a stainless steel grid and then mounted on a sample holder, which was specially designed for the FTIR transmission measurements, and the measurements were carried out over a large temperature region from 65 to 1000 K. The exposure of the samples to CO was carried out by backfilling the IR chamber up to 0.01 mbar at 105 K. The IR data were accumulated by recording 1024 scans with a resolution of 4 cm^{-1}. Before each exposure, a spectrum of the clean sample was recorded as a background reference.

Catalytic Tests. The catalytic properties were evaluated at 30 °C and 40 bar in a semicontinuous batch reactor (300 mL, Teflon inlay) equipped with a mechanical blowing stirrer (Teflon) and Teflon baffles. The semicontinuous batch reactor was conceived as a batch reactor in terms of the liquid phase with the suspended catalyst, while the gas phase ($H_2/O_2/N_2$ 4/20/76) was continuously supplied during the reaction (total flow 250 mL$_{NTP}$/min). The 4% amount of H_2 represents the lower flammability limit for H_2 in air and thus, for safety reasons, the H_2 concentration should never exceed 4% under these conditions.[54] It should be noted that the gas pressure was 40 bar and was constant over the reaction time. The supported catalysts (i.e., 1.3 mg of total metal content (Pd and Pb) per experiment) were suspended in ethanol (200 mL). Before the reaction was started, the slurry catalysts were activated with 4 vol % of H_2 in N_2 (250 mL$_{NTP}$/min (NTP, normal temperature and pressure), 30 °C and 40 bar), 1 h). The educt gas mixture (total flow 250 mL$_{NTP}$/min, gas composition $H_2/O_2/N_2$ 4/20/76) was introduced, and stirring was started (1000 rpm). The reactor was connected to a gas chromato graph (Inficon micro GC 3000) so that the H_2, O_2, and N_2 concentrations exiting the reactor could be periodically determined. N_2 was used as an internal standard to calculate H_2 and O_2 concentrations. Samples of the reaction mixture were periodically taken, and the H_2O_2 concentration ($c(H_2O_2)$) was analyzed after reaction with $TiOSO_4/H_2SO_4$ at a wavelength of 420 nm by UV−vis spectrometry (Specord S600, Analytik Jena). The H_2 conversion ($X(H_2)$) and the H_2O_2 selectivity ($S(H_2O_2)$) were determined after 63 min of reaction using eqs 1 and 2, respectively. Typically, all catalytic tests were performed twice and mean $S(H_2O_2)$, $X(H_2)$, and $P(H_2O_2)$ values were calculated. The mean statistical errors over all experiments were calculated to be 1.8% ($X(H_2)$), 5.6% ($S(H_2O_2)$), and 679 mol kg_{Pd}^{-1} h^{-1} ($P(H_2O_2)$). Stabilization

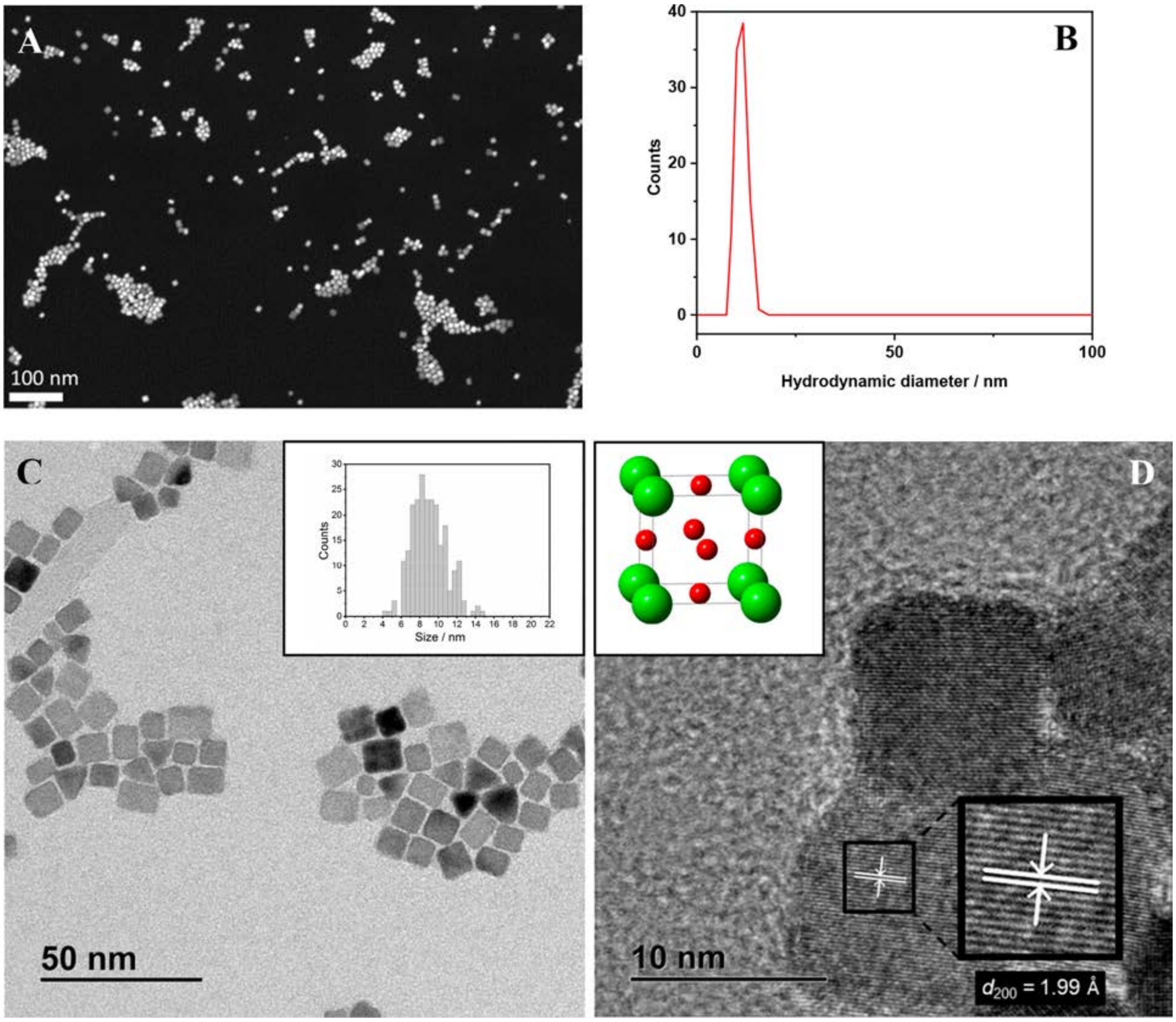

Figure 1. (A) Representative SEM image of Pd_3Pb cubes. (B) DLS analysis of Pd_3Pb cubes. (C) TEM image of Pd_3Pb cubes (inset: particle size distribution). (D) HRTEM image of Pd_3Pb cubes (inset: $L1_0$ Pd_3Pb structure with Pd shown in red and Pb in green).

of the gas mixture at the beginning of the reaction also contributes to the error with respect to $X(H_2)$ and $S(H_2)$.

$$X(H_2) = \frac{\text{consumed } H_2 \text{ (mol)}}{\text{inlet } H_2 \text{ (mol)}} \times 100\% \tag{1}$$

$$S(H_2O_2) = \frac{n(H_2O_2) \text{ (mol)}}{H_2 \text{ consumed (mol)}} \times 100\% \tag{2}$$

It should be noted that interphase transfer constraints can limit hydrogenation reactions in the three phase reaction system.[55] For a typical reaction and the investigated catalysts, mass transport may not be a dominant factor (see Figure S7 in the Supporting Information). However, we cannot exclude the possible effects of mass transfer limitations as being partially responsible for the observed differences in catalyst perform ance.

Computational Details. All calculations were performed using the VASP 5.4.1 package[56−59] with the Bayesian error estimation functional with van der Waals correction (BEEF vdW functional)[60,61] and the projector augmented wave (PAW) potentials.[62,63] The choice of the BEEF vdW func tional was motivated by its performance with regard to adsorption and transition state energies on transition metal surfaces.[64−66] Initially the bulk 2 × 2 × 2 supercell (32 atoms) was optimized and the obtained lattice cell parameters were used in further slab calculations. Exclusively 100 and 200 terminations (that correspond to cubic NCs) were studied. All built slabs consist of four layers; the two top layers were fully relaxed, while the two bottom layers were kept at their bulk positions. Two kinds of surfaces were investigated: (1) with Pb atoms in the top layer (normally noted as (100)) and (2) a Pd covered surface with Pb atoms in the sublayer (normally noted as (200)). Although the initial structures of these two surfaces had mirror symmetricy, the relaxation of top layers in the case of (200) decreases the energy more significantly than in case of the (100) surface. A Pd covered surface is hence preferable in comparison to the that with Pb in the top layer. This surface was investigated further and compared with Pd(100). An energy cutoff of 450 eV, (6 × 6 × 1) K point mesh, and 30 Å in the z direction (20 Å of vacuum) were used. The isolated molecules were structurally relaxed inside a large box of 15 × 15 × 15 Å (O_2 molecule with spin polarization, the energy of the H atom was taken as half of the energy of the H_2 molecule). The final TS structures were confirmed by a single

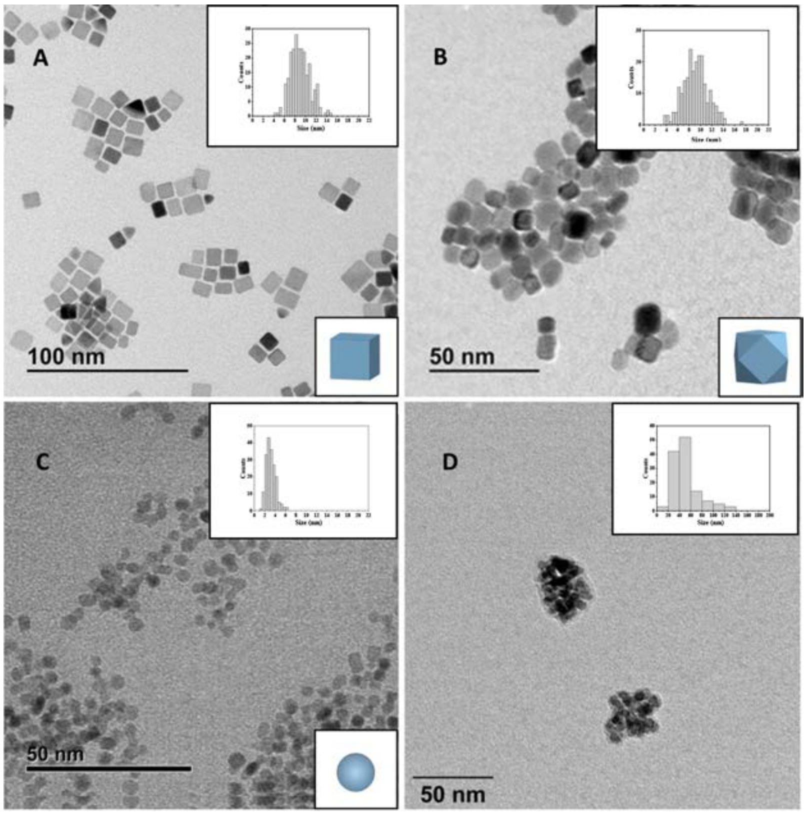

Figure 2. TEM images with particle size distributions of Pd_3Pb NCs: (A) Pd_3Pb cubes; (B) Pd_3Pb cuboctahedra; (C) Pd_3Pb spheres; (D) Pd_3Pb flowerlike aggregates.

imaginary frequency along the reaction coordinate calculated with a normal mode analysis.

RESULTS AND DISCUSSION

Pb doped NCs were prepared using a solution of palladium acetylacetonate ($Pd(acac)_2$) and lead acetylacetonate ($Pb(acac)_2$) in dioctyl ether. A mixture of OLAM, OLAC, and TOP was employed for the ligands. In the case of flowerlike aggregates, L ascorbic acid was employed instead of TOP. By a stepwise increase in the reaction temperature from 60 to 200 °C, the solution turned from pale yellow to black, indicating NC formation. The purified NCs were collected as a colloidal dispersion in chloroform. SEM and TEM images displayed mainly cubic shaped NCs with a size of 9.1(±1.9) nm (Figure 1 and Figure S1). High resolution TEM (HRTEM) images revealed the single crystalline character of the NCs with a lattice spacing of 0.199 nm, which is in good agreement with a $L1_0$ Pd_3Pb phase (0.202 nm for (200)) (Figure 1D and Figure S1B). DLS analysis revealed a hydrodynamic diameter of 15 nm and the absence of agglomerates or larger particles. An ICP OES analysis confirmed the presence of both metals in the NC powder and the bimetallic character of the NCs in a molar Pd/Pb ratio of 2.9/1, respectively (Table S1). We followed the NC formation during several steps of the NC synthesis by TEM analysis. Figure S2 shows the structural evolution of the NCs over the reaction time, where small spherical NCs (size 5.2(±1.2) nm) are initially formed (after 5 min of reaction at 200 °C) that then gradually transformed into cubic NCs after 40 min of reaction. We further investigated the influence of the different ligands on NC formation. It is well known that ligands control both NC nucleation and growth processes in solution and stabilize the as formed NCs. Ligands can passivate specific crystallographic facets, change their growth rates, and thereby induce the adsorbate controlled, shape selective NC formation. Alternatively, kinetic control may lead to the evolution of equilibrium shapes such as truncated octahedra by decreasing the production rate of metal monomers in solution. In the presence of TOP, pure Pd NCs were reported to nucleate at temperatures between 200 and 250 °C.[67−70] TOP was suggested to displace acac in the $Pd(acac)_2$ precursor, forming an intermediate $Pd^{II}(TOP)_4$ complex.[67,71] OLAM seemed to replace TOP in the Pd^{II} complex and to stabilize the final Pd^0 NCs.[67] OLAM may act as both a stabilizing ligand and a reducing agent. The addition of an ether such as benzyl ether in pure OLAM was shown to induce a change in morphology from spherical to cubic shaped NCs.[72] Recently, it has been further suggested that the initially formed Pd NCs control the decomposition of the second metal precursor, which is then successively alloyed to yield bimetallic NCs.[73]

Here, TOP was essential for the formation of Pd_3Pb cubes. When the reaction was carried out in the absence of TOP or with half of the TOP amount, Pd_3Pb NCs with less well defined corners and with a truncated cubic or cuboctahedral shape (referred to as Pd_3Pb cuboctahedra) or small NCs of spherical shape (Pd_3Pb spheres) were formed instead of cubes, respectively (Figure 2). The sizes of the Pd_3Pb cuboctahedra and Pd_3Pb spheres were 9.1(±2.2) and 3.4(±0.7) nm, respectively, according to a TEM analysis (Table S2). Addition of ascorbic acid instead of TOP under otherwise the same reaction conditions also prevented the formation of cubic NCs, and Pd_3Pb flowerlike aggregates were formed instead. It should be noted that ligands themselves may also influence the catalytic properties by steric hindrance, electronic interfacial effects, or selective blocking of surface sites.[74] Hexadecyl(2 hydroxyethyl)dimethylammonium dihydrogen phosphate li gands bound to Pd, for example, were reported to increase the energetic barrier for side reactions to water and thus result in increased H_2O_2 selectivity.[31] Recently, surface bound ligands were also suggested to interact with key intermediates favoring the H_2O_2 formation path and increasing selectivities.[75] The observed effect was most important for ligands with H bonding groups (i.e., alcohol groups), while the effect was less pronounced for OLAM or TOP. However, it cannot be completely excluded here that surface bound TOP partially contributes to the enhanced H_2O_2 selectivity and productivity. The formation of the intermetallic Pd_3Pb phase was preferred, and even if the molar Pd/Pb ratio was decreased from 3/1 to 2/1, Pd_3Pb NCs of cubic morphology were obtained. In addition, two types of monometallic Pd NCs with mean sizes of 4.8(±0.8) nm (Pd 4.8 NCs) and 7.2(±0.7) nm (Pd 7.2 NCs) were synthesized in the presence of OLAM and TOP, which were further used to prepare the Pd based reference catalysts (for details of the synthetic procedure and catalyst characterization see the Experimental Section, Tables S1−S3, and Figure S4 in the Supporting Information). It should be noted that the size distribution of Pd_3Pb cubes, Pd_3Pb cuboctahedra, and Pd_3Pb flowerlike aggregates (standard deviations of 1.9, 2.2, and 13.0 nm, respectively) was broader than that of the Pd_3Pb spheres and Pd NCs (standard deviations 0.7−0.8 nm) (Table S2).

The XRD patterns revealed broad reflections of low intensity that are characteristic for small NCs (Figure 3). For all NCs,

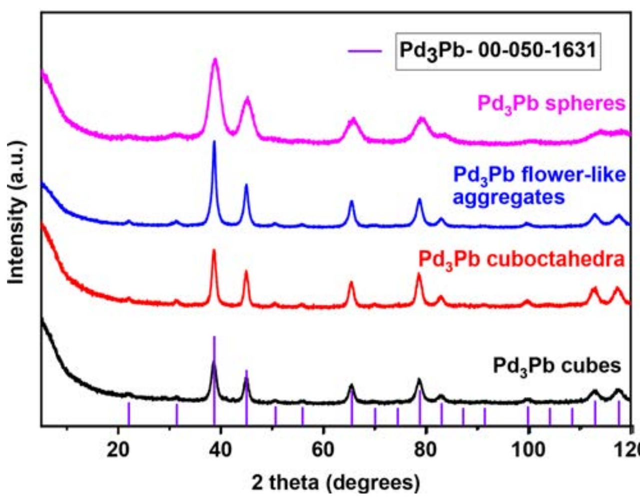

Figure 3. XRD analysis (Cu $K_{\alpha 1}$ radiation) of intermetallic Pd_3Pb particles with different shapes.

the reflections were consistent with the intermetallic Pd_3Pb $L1_0$ phase (ICDD 00 050 1631). The reflections were clearly shifted to lower Bragg angles due to the insertion of Pb atoms into the Pd lattice (ICDD 00 046 1043). For most samples, the XRD patterns also revealed superlattice reflections at 22.1, 31.4, 50.6, 55.9, 70.0, 74.2, 87.4, 91.2, 103.7, and 108.2° (2θ), which are characteristic for the ordered intermetallic $L1_0$ Pd_3Pb phase. For the Pd_3Pb spheres, however, superlattice reflections were very weak and hardly visible, indicating a lower degree of atomic ordering. The reflections of the correspond ing metal oxides (PbO, PbO_2, PdO) were not observed by an XRD analysis. However, we cannot exclude that a thin layer of metal oxide was formed after exposure of the NCs to air. Crystalllite sizes were calculated according to the Scherrer equation as 8.6 nm (Pd_3Pb cubes), 3.5 nm (Pd_3Pb spheres), 9.3 nm (Pd_3Pb cuboctahedra), and 8.7 nm (Pd_3Pb flowerlike aggregates) (Table S2), which are in good agreement with the NC sizes determined from TEM images (Table S2). According to the Scherrer equation, the crystallite size of the Pd_3Pb flowerlike aggregates was 8.7 nm and thus was comparable to the sizes of the Pd_3Pb cubes and Pd_3Pb cuboctahedra. However, the primary crystallites were aggregated into larger structures of approximately 36 nm (Table S2 and Figure S3). The crystallite sizes of the Pd NCs (Pd 4.8 NCs, 2.2 nm; Pd 7.2 NCs, 1.6 nm) was smaller than the sizes calculated on the basis of an TEM analysis, indicating a polycrystalline particle structure.

The Pd_3Pb NCs were adsorbed from a colloidal $CHCl_3$ dispersion onto the H_2SO_4 treated TiO_2 support (s TiO_2). In the direct H_2O_2 synthesis, various materials have been used to support the active metal phase (such as TiO_2,[33,44,76−78] Al_2O_3,[79] SiO_2,[36,80,81] ZrO_2,[82] Fe_2O_3, zeolites,[4,83] heteropolya cids,[84] and carbon based materials)[33,35,85] and it is well known that the support significantly influences the catalytic perform ance.[86] In particular, support materials with acidic properties (i.e., Brønsted acid sites) were reported to enhance selectivity and activity towards the direct synthesis of H_2O_2.[86,87] Here, commercial TiO_2 (P25, Evonik, 80% anatase/20% rutile, BET surface 54 m^2/g) was pretreated with H_2SO_4 to yield s TiO_2 (BET surface 52 m^2/g, (interparticle) BJH pore diameter 36 nm), which was chosen as a benchmark support material to compare the effect of metal doping and NC shape on the catalytic properties. The acid treatment of support materials was previously demonstrated to yield smaller active alloy Au Pd NPs and to switch off H_2O_2 hydrogenation/decomposition reactions, leading to enhanced H_2O_2 selectivity for Au Pd/C catalysts.[32] For sulfated titania [TiO_2/SO_4^{2-}], it has been also suggested that Lewis and Brønsted acid sites are induced on TiO_2 by binding of two oxygen atoms in SO_4^{2-} to Ti atoms.[88] Three weak, broad bands in the region between 1056 and 1222 cm^{-1} occur in the FTIR spectrum of s TiO_2 after treatment of TiO_2 (P25) with H_2SO_4 (2 wt %), which may be assigned to vibrational modes of bidentate sulfate ions in sulfated TiO_2 (Figure S6). H_2SO_4 pretreatment of the TiO_2 support also influences the pH value of the reaction medium, which may further promote direct H_2O_2 synthesis (Table S5). TEM images of the NCs immobilized on s TiO_2 showed that the NCs were well distributed over the s TiO_2 (Figure 4). After NC immobilization a slight decrease in the size of the Pd_3Pb cubes occurred (Table S2), which appears to be within the error of the measurement.

The structural and electronic properties of the surfaces exposed for s TiO_2 supported Pd NCs, Pd_3Pb cubes, and Pd_3Pb cuboctahedra were studied by UHV FTIR spectroscopy using CO as a probe molecule (Figure 5).

This extremely surface sensitive approach has been proven to be well suited to characterize oxide supported metals.[53,89,90] After CO adsorption at 105 K (Figure 5A), in addition to the CO vibration at about 2183 cm^{-1} being characteristic for the surface Ti^{4+} species, two IR bands are observed at 2150 and 2138 cm^{-1} for all three samples. They are assigned to CO species bound to Pd^{2+} cations that are formed via oxidation of surface Pd with oxygen at room temperature.[91] For pure Pd NCs, the spectrum displays two broad low frequency features centered at 1975 and 1925 cm^{-1} originating from CO

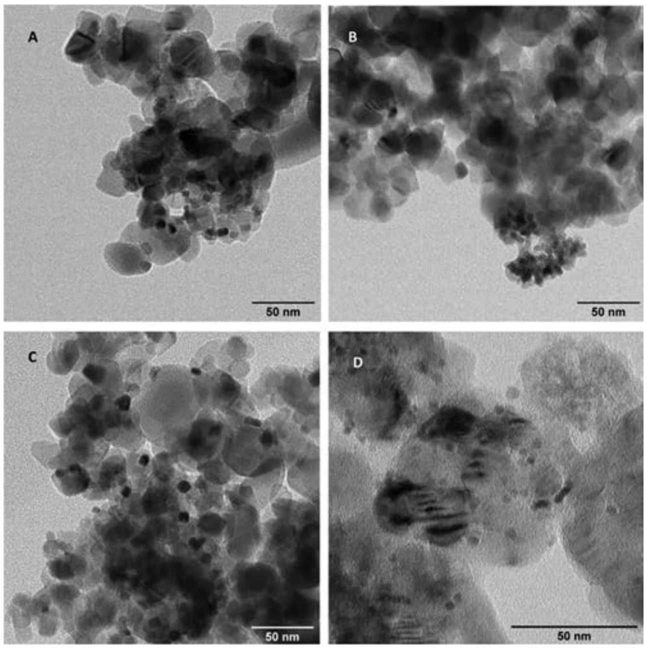

Figure 4. TEM images of Pd_3Pb NCs supported on s TiO_2: (A) Pd_3Pb cubes/s TiO; (B) Pd_3Pb flowerlike aggregates/s TiO_2; (C) Pd_3Pb cuboctahedra/s TiO_2; (D) Pd_3Pb spheres/s TiO_2 (c_1: total metal loading 13.8 wt %).

molecules adsorbed to surface Pd sites in a bridging configuration.[91] It is known that CO prefers to adsorb at bridge sites on Pd surfaces with a higher binding energy. This is confirmed by the temperature dependent IR results (see Figure 5B), where the two bridge Pd related CO signals are rather stable and become the dominating bands upon annealing to 350 K. Furthermore, a new CO band appears at 2100 cm^{-1}, which is attributed to CO bonded linearly to Pd^0 atop sites.[91] As was observed for pure Pd NCs, the temperature dependent IR spectra for Pd_3Pb cuboctahedra (Figure 5C) and Pd_3Pb cubes (Figure 5D) reveal the presence of various CO species bound to metallic Pd^0 atop and bridge sites. The identification of surface metallic Pd sites can be explained in terms of (i) reduction of surface Pd^{2+} to Pd^0 via CO oxidation at elevated temperatures and (ii) thermal diffusion of CO species to the more stable metal sites. Importantly, for Pd_3Pb cuboctahedra the IR band of CO bound to surface Pd^0 atop sites (2102 cm^{-1}) remains nearly unchanged in frequency in comparison to that for pure Pd NCs (2100 cm^{-1}), whereas in the case of Pd_3Pb cubes the atop Pd^0 related CO vibration shows a significant blue shift to 2115 cm^{-1} (see Figure 5D). These findings allow us to gain insights into the electronic modification of surface Pd atoms exposed by differently shaped Pd_3Pb nanoalloys. The large frequency shift observed for Pd_3Pb cubes reveals that its surface is predominantly terminated by intermetallic Pd atoms, where the charge transfer occurs between Pd and Pb due to strong electronic interactions induced by the large electronegativity difference.[92] The presence of intermetallic Pd atoms is supported by the observation of weak IR bands in the region of CO bound to bridge Pd^0 sites (Figure 5D), indicating the lack of Pd ensembles on Pd_3Pb cube surfaces. In contrast, for Pd_3Pb cuboctahedra the bridge Pd^0 related CO vibration at about 1900 cm^{-1} is detected as an intense and dominant band at 375 K (Figure 5C), revealing that the surface is enriched with Pd atoms. The small frequency shift of the atop Pd^0 CO in comparison to pure Pd NCs provides further evidence that the monometallic Pd atoms are the major species exposed by the surface of Pd_3Pb cuboctahedra. It should be noted that single Pd sites were suggested to preferentially form H_2O_2, while groupings of Pd atoms formed H_2O instead.[45] This is in good agreement with the enhanced H_2O_2 selectivity that was observed for our Pd_3Pb cubes (see below).

There has been a great interest in enhancing the catalytic performance and/or decreasing the costs of the noble metal based catalysts (Pd, Pt, Au) by introducing cost effective, non noble metal dopants.[93,39,36] In particular, NCs with ordered, intermetallic composition are highly attractive since they may reveal enhanced catalytic performance and chemical stability.[38,94,95] Recently, Pd_3Pb tripods, for example, have been reported to enhance the four electron oxygen reduction electrocatalysis.[96] The catalytic performance of the supported Pd_3Pb NCs in the direct H_2O_2 synthesis was determined in a semicontinuous batch reactor (gas composition $H_2/O_2/N_2$ 4/20/76; 30 °C; 40 bar; solvent ethanol; total metal content (Pd and Pb) 1.3 mg) with s TiO_2 supported Pd NCs (mean NC sizes 4.8 ± 0.8 and 7.2 ± 0.7 nm) as reference catalysts. It should be noted that the reaction medium significantly influences the reaction rates and H_2O_2 selectivity in the direct H_2O_2 synthesis and a number of different solvents have been investigated, including water, methanol, and ethanol.[19] The preferred solvent may depend on the downstream application of H_2O_2. While the use of H_2O_2 as a bleaching agent for pulp and textiles favors the use of H_2O_2 diluted in water, solvents of simple alcohols (e.g., methanol or ethanol) are preferable if H_2O_2 is employed as an oxygen source in epoxidation or oxidation reactions. While water is nontoxic and nonflammable, it also has a relatively low solubility of H_2 (1.62 mg/mL or 0.81 mM at 25 °C) and O_2 (40 mg/mL or 1.25 mM at 25 °C). Ethanol has a 5 fold larger H_2 solubility (7.50 mg/mL; 3.75 mM) and an 8 fold greater O_2 solubility (320 mg/mL; 10.0 mM). The rate dependences and kinetic behaviors for H_2O_2 formation were shown to differ significantly for alcohol and aprotic solvents, suggesting that the solvent also participates directly in the catalytic cycle.[19,26] Due to a heterolytic proton transfer mechanism, H_2O_2 formation was only observed in the presence of protic solvents and was not detected in aprotic solvents. Ethanol and acetic acid (added or produced *in situ*) were also suggested to be responsible for enhanced H_2O_2 selectivities in ethanol vs water solvent.

The hydrogen conversion ($X(H_2)$) was 36% for the intermetallic Pd_3Pb cubes/s TiO_2 catalyst and was similar for the monometallic Pd/s TiO_2 reference catalysts ($X(H_2$; Pd 4.8/s TiO_2), 35%; $X(H_2$; Pd 7.2/s TiO_2), 42%) (Figure 6A and Table S6) (for details of Pd NC preparation and characterization, see the Supporting Information). Doping of Pd NCs with Pb in intermetallic Pd_3Pb cubes/s TiO_2, however, clearly enhanced the H_2O_2 selectivity and productivity ($S(H_2O_2$: Pd 4.8/s TiO_2), 21%; $S(H_2O_2$; Pd 7.2/s TiO_2), 25%; $S(H_2O_2$; Pd_3Pb cubes/s TiO_2), 53%; $P(H_2O_2$; Pd 4.8/s TiO_2), 1530 mol(H_2O_2) kg_{Pd}^{-1} h^{-1}; $P(H_2O_2$; Pd 7.2/s TiO_2), 2213 mol(H_2O_2) kg_{Pd}^{-1} h^{-1}; $P(H_2O_2$; Pd_3Pb cubes/s TiO_2), 7339 mol(H_2O_2) kg_{Pd}^{-1} h^{-1}) (Figure 6B,C and Table S4). For all other types of NC morphologies, $X(H_2)$ decreased in comparison to the Pd/s TiO_2 reference while $S(H_2O_2)$ also increased ($S(H_2O_2)$: 49% (Pd_3Pb cuboctahedra/s TiO_2); 41% (Pd_3Pb flowerlike aggregates/s TiO_2)) (Figure 6 and Table S4). In the case of the Pd_3Pb cuboctahedra/s TiO_2

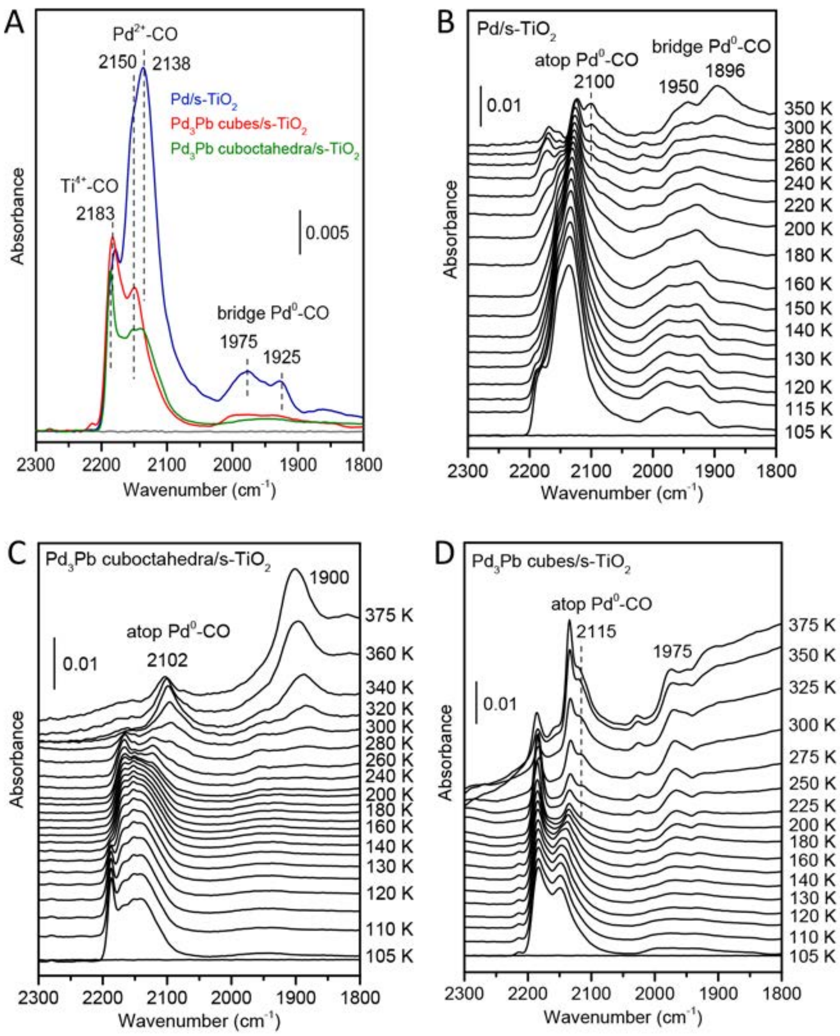

Figure 5. (A) Infrared spectra obtained after CO adsorption (0.01 mbar) at 105 K on Pd/s TiO_2, Pd_3Pb cuboctahedra/s TiO_2, and Pd_3Pb cubes/s TiO_2 samples. Temperature dependent IR spectra of CO adsorbed on (B) Pd/s TiO_2, (C) Pd_3Pb cuboctahedra/s TiO_2, and (D) Pd_3Pb cubes/s TiO_2.

and Pd_3Pb flowerlike aggregates/s TiO_2 catalysts the H_2O_2 productivities were 4218 and 3242 $mol_{H_2O_2}$ kg_{Pd}^{-1} h^{-1} (Table S4), respectively, and were still higher than for the monometallic Pd reference catalysts. For Pd_3Pb with spherical shape (Pd_3Pb spheres/s TiO_2 (c_1): total metal loading 13.8 wt %), the overall H_2O_2 productivity (761 $mol_{H_2O_2}$ kg_{Pd}^{-1} h^{-1}) and $X(H_2)$ (9%) remained low (Table S4). When the metal loading was reduced (Pd_3Pb spheres/s TiO_2 (c_2): total metal loading 4.0 wt %), H_2 conversion ($X(H_2)$ 22%) and H_2O_2 productivity (1163 mol kg_{Pd}^{-1} h^{-1}) remained below those of the Pd NC reference catalysts while H_2O_2 selectivity ($S(H_2O_2)$ 24%) was comparable to that of one of the Pd reference catalysts. This observation may result from the morphology, small size, and/or some Pb segregation on the NC surface of the Pd_3Pb spheres. A decrease in $X(H_2)$ and H_2O_2 productivity was recently also observed for s TiO_2 supported, spherical Pd/Pb based NCs (size 5.6 nm) that were prepared by a different synthetic approach (Table S6).[38] H_2O_2 production appears to be dependent on particle shape: i.e., Pd_3Pb cubes seemed to outperform not only the Pd/s TiO_2 catalyst but also Pd_3Pb particles with a cuboctahedral, spherical, or flowerlike morphology. Figure 6D compares the concentration of H_2O_2 over reaction time for all Pb doped Pd catalysts, illustrating that Pd_3Pb cubes outperformed Pd_3Pb NCs with other morphologies. TEM and SEM images of the spent catalysts after the catalytic reaction are shown for selected catalysts (i.e., Pd_3Pb cubes/s TiO_2 and Pd 7.2/s TiO_2 reference catalyst) in Figure S5. On the basis of these images, there appears to be no evidence for NC reconstruction under the present conditions of catalyst testing. It should be noted that possible effects of mass transport limitations may also influence the observed differences in catalytic behavior and cannot be excluded. An evaluation of the catalytic H_2O_2 selectivity and productivity is given in Table S6 (with details of the reaction parameters). Previously, the modification of Pd by the addition of a range of precious or nonprecious metals (in particular Sn) was demonstrated to enhance catalytic H_2O_2 selectivity and productivity. In accordance with these studies, we now report that not only the addition of Pb but also the nature of the exposed surface facets in s TiO_2 supported Pd_3Pb cubes further improves H_2O_2 selectivity and, importantly, leads to a enhanced H_2O_2 productivity. Recently, alloyed Pd Pb particles have been suggested as promising substitutes for Au Pd in the direct H_2O_2 synthesis by a combination of density functional theory calculations and Sabatier analysis.[50] The average

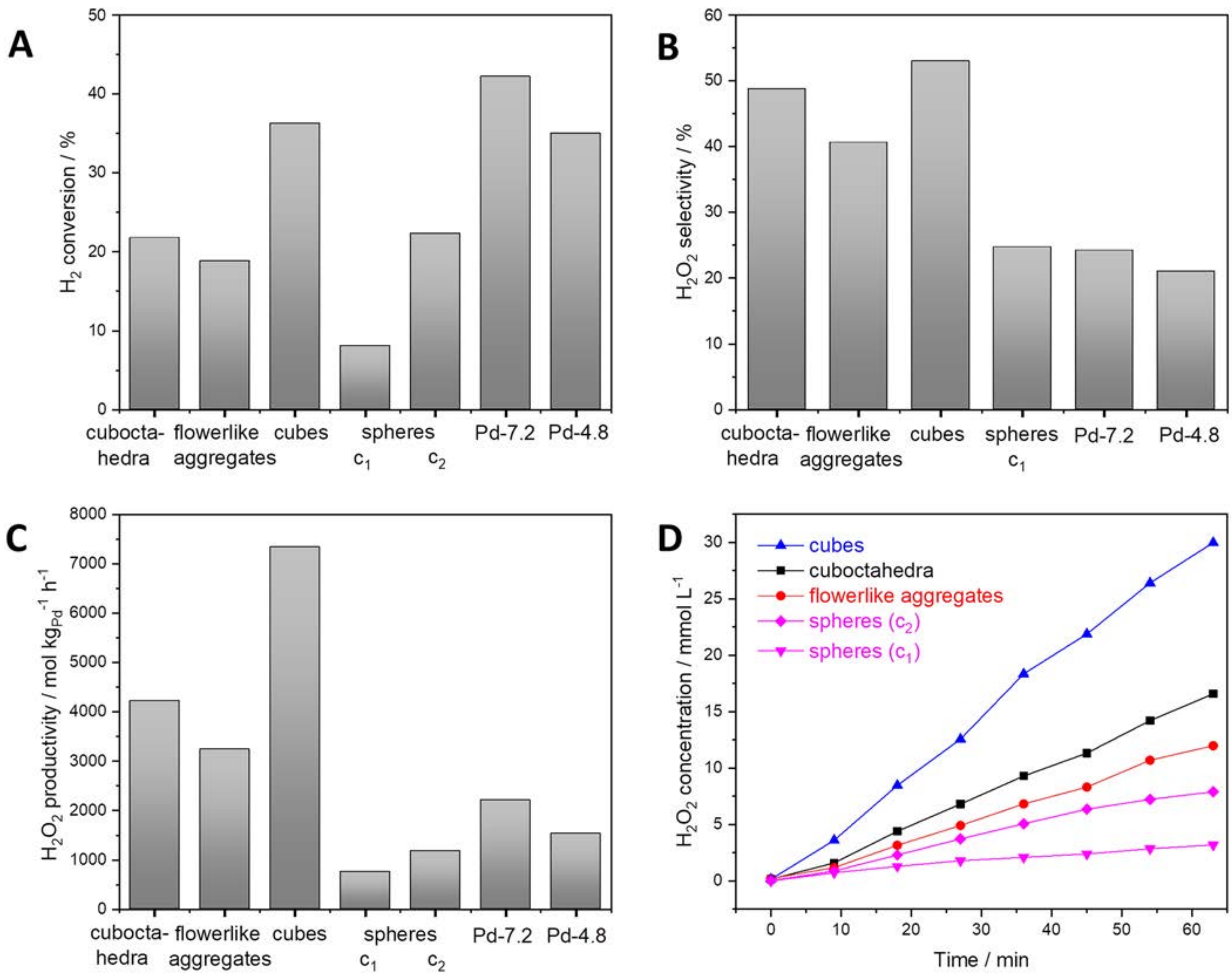

Figure 6. Catalytic performance of the s TiO_2 supported Pd_3Pb NC catalysts (i.e. cuboctahedra (Pd_3Pb cuboctahedra/s TiO_2), flowerlike aggregates (Pd_3Pb flowerlike aggregates/s TiO_2), cubes (Pd_3Pb cubes/s TiO_2; spheres), Pd_3Pb spheres/s TiO_2 with 13.8 wt % (c_1) and 4 wt % metal loading) depending on the catalyst morphology. Reaction conditions: 40 bar, 30 °C, ethanol, gas composition $H_2/O_2/N_2$ 4/20/76, total flow 250 mL_{NTP}/min. Monometallic, spherical Pd NCs (Pd 7.2/s TiO_2 (i.e., Pd 7.2), mean size based on TEM images 7.2 ± 0.7 nm; Pd 4.8/s TiO_2 (i.e., Pd 4.8), mean size based on TEM images 4.8 ± 0.7 nm) were used as precursors to prepare reference catalysts. (A) H_2 conversion, (B) H_2O_2 selectivity ,and (C) H_2O_2 productivity of the catalysts in the direct synthesis of H_2O_2. (D) Concentration of H_2O_2 produced as a function of time.

number of valence electrons of Pd shell atoms seemed to determine the activity and selectivity of the Pd based nanocatalysts, which was tuned by the electronegativity of the Pb dopant. Our experimental studies showed that the properties of the Pd_3Pb NCs are more complex and the experimental catalytic properties seemed to be also shape dependent with an enhanced $X(H_2)$, $S(H_2O_2)$, and H_2O_2 productivity observed especially for the cubic shaped Pd_3Pb particles. As shown by UHV FTIR studies (Figure 5), the surface of s TiO_2 supported Pd_3Pb cubes further revealed a lack in Pd ensemble sites together with the strong electronic modification of the Pd surface atoms. Figure 1D and Figure S1 show HRTEM images of the Pd_3Pb cubes which preferentially expose the (200) facets. Not only electronic effects but also the specific geometry of the Pd surface sites observed in Pd_3Pb cubes could have contributed here to the enhanced catalytic properties. For transition metal nanocrystals, facet dependent catalytic properties have been elaborated in a large number of catalytic reactions.[97] For monometallic Pd NCs, the (111) facets exposed by Pd nanooctahedra, for example, were shown to be more favorable than the (100) facets of Pd nanocubes with respect to $S(H_2O_2)$ and reaction rate in the direct synthesis of H_2O_2.[28,98,28] H_2 conversion and H_2O_2 selectivity were just recently further improved by depositing Pt on Pd cubes, which preferentially grew on the corners and edges of the Pd cubes and led to the formation of concave structures.[47] High H_2O_2 selectivity was achieved for deposition of Pt/Au on Pd cubes in a 3.75/3.75 mol % ratio, but the H_2 conversion decreased at the same time.[99] Au on Pd terrace sites was suggested to contribute to selective H_2O_2 production, while Pt sites on the corners and edges facilitated H_2 conversion.

We performed DFT calculations to shed light on the reason behind the H_2O_2 selectivity observed for Pd_3Pb NCs (see the Supporting Information for all structures and related energies). Our DFT calculations show that Pd_3Pb preferably has a Pd covered surface. We focus on Pd and Pd_3Pb surfaces rather than PdH phases, as these have been shown not to exist under the reaction conditions applied here.[100] We investigated the reaction of O_2 with H_2 on the Pd covered Pd_3Pb surface, $Pd_3Pb(200)$, in comparison to Pd(100). The free energy diagram at 303 K is shown in Figure 7. In general, the

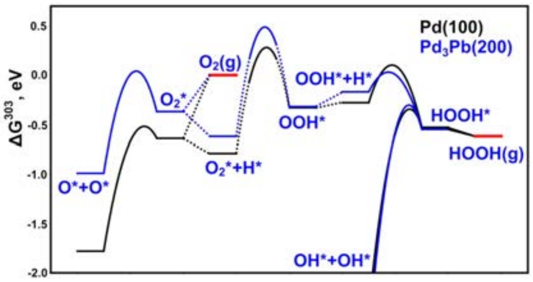

Figure 7. Reaction mechanism (Gibbs free energy diagram at 303 K) of H_2O_2 synthesis on Pd(100) (black line) and $Pd_3Pb(200)$ (blue line) surfaces. Dotted lines correspond to absorption processes on the surface. All energies are referenced to O_2 and H_2 in the gas phase.

characteristics of the pathway are similar to those that have been found in earlier theoretical studies not only for Pd(100)[101−104] but also for other surfaces such as Pt(100)[105] as well as $Pt_3Ni(100)$ and Pt/Cu(100).[106] O_2 adsorption is exothermic by 0.37 and 0.64 eV on $Pd_3Pb(200)$ and Pd(100), respectively. Likewise, dissociation of adsorbed O_2 has a lower barrier on Pd(100) (0.12 eV) in comparison to that on $Pd_3Pb(200)$ (0.41 eV). Hydrogenation of OOH has comparatively high barriers, being 1.11 and 1.07 eV on $Pd_3Pb(200)$ and Pd(100), respectively. Hydrogenation of the OOH* intermediate to H_2O_2, on the other hand, has rather low barriers. The desorption of formed H_2O_2 is exothermic at 303 K, whereas splitting of adsorbed H_2O_2 to two hydroxyl groups has a small barrier. The main finding is that the differences between the splitting of O_2* and its hydrogenation to OOH* are larger for $Pd_3Pb(200)$ by 0.35 eV in comparison to Pd(100), in line with the increase in selectivity observed experimentally. While this trend confirms the experimental findings and rationalizes them by the weaker binding of intermediates and transition states to $Pd_3Pb(200)$ in comparison to Pd(100), we note that a deeper analysis of the selectivity of $Pd_3Pb(200)$ requires more elaborate kinetic analyses. We also note that, while the functional employed here has been found to exhibit errors for adsorption energies and transition states in the range of ±0.2 eV, this study does not include the effect of the solvent and possible higher surface coverages of oxygen. Solvent effects using water have been shown to stabilize OOH* and OH* by about 0.25 and 0.5 eV, respectively, thus potentially decreasing the adsorption energy of OOH* and the associated hydrogenation barrier.[107,108] Other mechanisms such as the recombination of 2 OH* to H_2O_2 are not considered herein, as they have been ruled out by isotope labeling experiments.[109] Other routes for hydrogen addition have been found to be higher in energy (see Figure S11). We also note that the mechanism presented herein is based on the homolytic cleavage of hydrogen and the surface reaction of O_2 and OOH with adsorbed H*. While the heterogeneous nature of the reaction investigated here is rather different from the electrochemical synthesis of H_2O_2 that involves proton/electron transfer processes, there have been suggestions in the literature that the same applies for heterogeneous H_2O_2 synthesis in protic solvents.[19,22] Since coupled electron/proton transfer leads to the same intermediates calculated herein, we expect that the trends observed here will be similar to those for alternative mechanisms.

We calculated the adsorption enthalpies of gas phase ethanol on Pd(100) and $Pd_3Pb(200)$ surfaces to be −0.47 and −0.33 eV. When they are referenced to liquid ethanol, we conclude that the coverage of ethanol on surfaces is negligible (see the Supporting Information for an in depth discussion). Additionally, the effects of oxygen and bromine to the O_2 dissociation barrier have been analyzed (see Figure S10). Importantly, we observe that the barriers increase by approximately the same amount for both surfaces considered herein as a function of surface coverage. We thus conclude that the trend obtained for the low coverage regime holds for higher coverages as well.

CONCLUSIONS

Intermetallic Pd_3Pb NCs with sizes in the 3.4−9.1 nm range and different shapes were produced using a facile synthesis route, and their size, shape, composition, and surface properties were studied by a combination of TEM, XRD, and FTIR using CO as a probe molecule. For catalytic testing, the NCs were immobilized on acid pretreated TiO_2 and their catalytic performance was tested in the direct synthesis of H_2O_2.

The addition of TOP had a strong effect on the NC shape, and in the absence of TOP, no cubic particles were formed. Instead, small spherical NCs or cuboctahedra were obtained if the amount of TOP was reduced by half or no TOP was used, respectively. Structural and chemical information shows that the NCs form an ordered intermetallic $L1_0$ Pd_3Pb phase with a Pb content close to that of the Pd_3Pb composition. Although Pb is well known to modify the selectivity of Pd sites, e.g., in Lindlar catalysts, this is also the first experimental evidence for the promotional effects of Pb doping in Pd catalysts for direct H_2O_2 synthesis. Our catalytic tests show that the H_2O_2 selectivity may be enhanced by Pb doping of Pd catalysts in direct H_2O_2 synthesis. H_2 conversion and H_2O_2 selectivity and production, however, were not only affected by NC composition but also appeared to depend on the particle shape. Pd_3Pb cubes outperformed not only the Pd/s TiO_2 catalyst but also Pd_3Pb particles with a cuboctahedral, spherical, or flowerlike morphology. Pd_3Pb cubes revealed a high H_2O_2 selectivity while maintaining also a high H_2 conversion, resulting in a H_2O_2 productivity of 7339 mol kg_{Pd}^{-1} h^{-1}. Pd_3Pb NCs with a cubic shape were predominantly terminated by their (200) facets. DFT calculations showed that the dissociation of adsorbed O_2 has a lower barrier on Pd (100) in comparison to Pd_3Pb (200), in line with the selectivity increase to H_2O_2 observed experimentally. Notably, UHV FTIR spectra of adsorbed CO also revealed significant differences in Pd surface sites for Pd_3Pb cubes and monometallic Pd particles. A significant blue shift of the atop Pd^0 related CO vibration together with only weak IR bands in the region of CO bound to Pd^0 bridge sites indicated not only the electronic modification of Pd surface atoms but also the lack of Pd ensembles in Pd_3Pb NCs with a cubic shape. This could be the reason that the high catalytic activity of Pd in direct H_2O_2 synthesis was maintained for Pd_3Pb cubes together with an unusually high catalytic selectivity.

Overall, further enhancement of the catalytic performance may be expected by further improvements of the reactor setup and optimization of the reaction conditions. In general, the influence of the numerous reaction variables and materials parameters is complex and their influence on the catalytic performance in this reaction is not well understood. Therefore, insights into structure−performance relationships may contribute to a future understanding of the influence of the material parameters on the overall catalytic behavior and to a more rational catalyst design.

Experimental details on the synthesis of the Pd reference NCs including TEM images, size histograms, and an XRD analysis, details of reaction conditions for the NC synthesis, size of the NC before/after deposition on a s TiO$_2$ support (based on TEM/XRD analysis), influence of acid washed TiO$_2$ (s TiO$_2$) on the pH value of reaction medium, FTIR spectrum of s TiO$_2$, NC and catalyst compositions, H_2 conversions, H_2O_2 selectivities, and H_2O_2 productivities, reference to literature catalysts with reaction conditions, Gibbs free energies and enthalpies for the formation of reaction intermediates, TEM/HRTEM images of Pd_3Pb nanocubes and flowerlike aggregates, transition state of O_2 dissociation on the $Pd_3Pb(200)$ surface, reaction barriers for O_2 dissociation on the Pd(100) surface with different coadsorbed species, and additional information on the reaction mechanism (PDF)

AUTHOR INFORMATION

Corresponding Author

Silke Behrens − *Institute of Catalysis Research and Technology, Karlsruher Institut für Technologie, D 76344 Eggenstein Leopoldshafen, Germany; Institute of Inorganic Chemistry, Ruprecht Karls University Heidelberg, D 69120 Heidelberg, Germany;* orcid.org/0000 0003 4328 9564; Email: silke.behrens@kit.edu

Authors

Vanitha Reddy Naina − *Institute of Catalysis Research and Technology, Karlsruher Institut für Technologie, D 76344 Eggenstein Leopoldshafen, Germany; Catalysis Group, Department of Chemistry, Indian Institute of Technology Indore, Indore 453552, Madhya Pradesh, India*

Sheng Wang − *Institute of Catalysis Research and Technology, Karlsruher Institut für Technologie, D 76344 Eggenstein Leopoldshafen, Germany; Institute of Inorganic Chemistry, Ruprecht Karls University Heidelberg, D 69120 Heidelberg, Germany*

Dmitry I. Sharapa − *Institute of Catalysis Research and Technology, Karlsruher Institut für Technologie, D 76344 Eggenstein Leopoldshafen, Germany;* orcid.org/0000 0001 9510 9081

Michael Zimmermann − *Institute of Catalysis Research and Technology, Karlsruher Institut für Technologie, D 76344 Eggenstein Leopoldshafen, Germany*

Martin Hähsler − *Institute of Catalysis Research and Technology, Karlsruher Institut für Technologie, D 76344 Eggenstein Leopoldshafen, Germany; Institute of Inorganic Chemistry, Ruprecht Karls University Heidelberg, D 69120 Heidelberg, Germany;* orcid.org/0000 0002 2352 5286

Lukas Niebl Eibenstein − *Institute of Catalysis Research and Technology, Karlsruher Institut für Technologie, D 76344 Eggenstein Leopoldshafen, Germany*

Junjun Wang − *Institute of Functional Interfaces, Karlsruher Institut für Technologie, D 76344 Eggenstein Leopoldshafen, Germany*

Christof Wöll − *Institute of Functional Interfaces, Karlsruher Institut für Technologie, D 76344 Eggenstein Leopoldshafen, Germany;* orcid.org/0000 0003 1078 3304

Yuemin Wang − *Institute of Functional Interfaces, Karlsruher Institut für Technologie, D 76344 Eggenstein Leopoldshafen, Germany;* orcid.org/0000 0002 9963 5473

Sanjay Kumar Singh − *Catalysis Group, Department of Chemistry, Indian Institute of Technology Indore, Indore 453552, Madhya Pradesh, India;* orcid.org/0000 0002 8070 7350

Felix Studt − *Institute of Catalysis Research and Technology, Karlsruher Institut für Technologie, D 76344 Eggenstein Leopoldshafen, Germany; Institute for Chemical Technology and Polymer Science, Karlsruher Institut für Technologie, D 76131 Karlsruhe, Germany;* orcid.org/0000 0001 6841 4232

Author Contributions

⊥V.R.N. and S.W. contributed equally.

Notes

The authors declare no competing financial interest.

ACKNOWLEDGMENTS

We thank Yannick Träutlein, Angelika Kahrau, Sarah Essig, Doreen Neumann Walter, Jan Eckel and Ioana Ciubotaru for experimental support. D.I.S. and F.S. acknowledge support by the state of Baden Württemberg through bwHPC (bwUniclus ter and JUSTUS, RV bw17D01). The authors would like to acknowledge the VirtMat project as well as support from the Helmholtz Association.V.R.N. acknowledges her scholarship in the DAAD India IIT Master Sandwich Programme (IIT), 2018 (57434206).

ABBREVIATIONS

NC, nanocrystal; s TiO$_2$, TiO$_2$ pretreated with H_2SO_4 (2 wt %)

REFERENCES

(1) Campos Martin, J. M.; Blanco Brieva, G.; Fierro, J. L. Hydrogen Peroxide Synthesis: An Outlook beyond the Anthraquinone Process. *Angew. Chem., Int. Ed.* **2006**, *45* (42), 6962−84.

(2) Wilson, N. M.; Bregante, D. T.; Priyadarshini, P.; Flaherty, D. W. Production and Use of H_2O_2 for Atom efficient Functionalization of Hydrocarbons and Small Molecules. *Catalysis* **2017**, *29*, 122−212.

(3) Melchionna, M.; Fornasiero, P.; Prato, M. The Rise of Hydrogen Peroxide as the Main Product by Metal Free Catalysis in Oxygen Reductions. *Adv. Mater.* **2019**, *31* (13), 1802920.

(4) Lewis, R. J.; Hutchings, G. J. Recent Advances in the Direct Synthesis of H_2O_2. *ChemCatChem* **2019**, *11* (1), 298−308.

(5) Yang, S.; Verdaguer Casadevall, A.; Arnarson, L.; Silvioli, L.; Čolić, V.; Frydendal, R.; Rossmeisl, J.; Chorkendorff, I.; Stephens, I. E. L. Toward the Decentralized Electrochemical Production of H_2O_2: A Focus on the Catalysis. *ACS Catal.* **2018**, *8* (5), 4064−4081.

(6) Jirkovský, J. S.; Panas, I.; Ahlberg, E.; Halasa, M.; Romani, S.; Schiffrin, D. J. Single Atom Hot Spots at Au−Pd Nanoalloys for

Electrocatalytic H_2O_2 Production. *J. Am. Chem. Soc.* **2011**, *133* (48), 19432−19441.
(7) Pizzutilo, E.; Freakley, S. J.; Cherevko, S.; Venkatesan, S.; Hutchings, G. J.; Liebscher, C. H.; Dehm, G.; Mayrhofer, K. J. J. Gold−Palladium Bimetallic Catalyst Stability: Consequences for Hydrogen Peroxide Selectivity. *ACS Catal.* **2017**, *7* (9), 5699−5705.
(8) Verdaguer Casadevall, A.; Deiana, D.; Karamad, M.; Siahrostami, S.; Malacrida, P.; Hansen, T. W.; Rossmeisl, J.; Chorkendorff, I.; Stephens, I. E. L. Trends in the Electrochemical Synthesis of H_2O_2: Enhancing Activity and Selectivity by Electrocatalytic Site Engineer ing. *Nano Lett.* **2014**, *14* (3), 1603−1608.
(9) Siahrostami, S.; Verdaguer Casadevall, A.; Karamad, M.; Deiana, D.; Malacrida, P.; Wickman, B.; Escudero Escribano, M.; Paoli, E. A.; Frydendal, R.; Hansen, T. W.; Chorkendorff, I.; Stephens, I. E. L.; Rossmeisl, J. Enabling Direct H_2O_2 Production through Rational Electrocatalyst Design. *Nat. Mater.* **2013**, *12* (12), 1137−1143.
(10) Han, L.; Sun, Y.; Li, S.; Cheng, C.; Halbig, C. E.; Feicht, P.; Hübner, J. L.; Strasser, P.; Eigler, S. In Plane Carbon Lattice Defect Regulating Electrochemical Oxygen Reduction to Hydrogen Peroxide Production over Nitrogen Doped Graphene. *ACS Catal.* **2019**, *9* (2), 1283−1288.
(11) Kim, H. W.; Ross, M. B.; Kornienko, N.; Zhang, L.; Guo, J.; Yang, P.; McCloskey, B. D. Efficient Hydrogen Peroxide Generation Using Reduced Graphene Oxide based Oxygen Reduction Electro catalysts. *Nature Catalysis* **2018**, *1* (4), 282−290.
(12) Liu, W.; Chen, Y.; Qi, H.; Zhang, L.; Yan, W.; Liu, X.; Yang, X.; Miao, S.; Wang, W.; Liu, C.; Wang, A.; Li, J.; Zhang, T. A Durable Nickel Single Atom Catalyst for Hydrogenation Reactions and Cellulose Valorization under Harsh Conditions. *Angew. Chem., Int. Ed.* **2018**, *57* (24), 7071−7075.
(13) Siahrostami, S.; Villegas, S. J.; Bagherzadeh Mostaghimi, A. H.; Back, S.; Farimani, A. B.; Wang, H.; Persson, K. A.; Montoya, J. A Review on Challenges and Successes in Atomic Scale Design of Catalysts for Electrochemical Synthesis of Hydrogen Peroxide. *ACS Catal.* **2020**, *10* (14), 7495−7511.
(14) Xia, C.; Xia, Y.; Zhu, P.; Fan, L.; Wang, H. Direct Electrosynthesis of Pure Aqueous H_2O_2 Solutions up to 20% by Weight Using a Solid Electrolyte. *Science* **2019**, *366* (6462), 226−231.
(15) Fukuzumi, S.; Yamada, Y. Hydrogen Peroxide used as a Solar Fuel in One Compartment Fuel Cells. *ChemElectroChem* **2016**, *3* (12), 1978−1989.
(16) Mase, K.; Yoneda, M.; Yamada, Y.; Fukuzumi, S. Seawater Usable for Production and Consumption of Hydrogen Peroxide as a Solar Fuel. *Nat. Commun.* **2016**, *7* (1), 11470.
(17) Wilson, N. M.; Bregante, D. T.; Priyadarshini, P.; Flaherty, D. W. Production and Use of H_2O_2 for Atom efficient Functionalization of Hydrocarbons and Small Molecules. *Catalysis* **2017**, *29*, 122−212.
(18) Henkel, H.; Weber, W. Manufacture of hydrogen peroxide. US Patent US1108752A, . 1914.
(19) Flaherty, D. W. Direct Synthesis of H_2O_2 from H_2 and O_2 on Pd Catalysts: Current Understanding, Outstanding Questions, and Research Needs. *ACS Catal.* **2018**, *8* (2), 1520−1527.
(20) Freakley, S. J.; Kochius, S.; van Marwijk, J.; Fenner, C.; Lewis, R. J.; Baldenius, K.; Marais, S. S.; Opperman, D. J.; Harrison, S. T. L.; Alcalde, M.; Smit, M. S.; Hutchings, G. J. A Chemo enzymatic Oxidation Cascade to Activate C−H Bonds with in situ Generated H_2O_2. *Nat. Commun.* **2019**, *10* (1), 4178.
(21) Liu, Q.; Lunsford, J. H. The Roles of Chloride Ions in the Direct Formation of H_2O_2 from H_2 and O_2 over a Pd/SiO_2 Catalyst in a H_2SO_4/ethanol System. *J. Catal.* **2006**, *239* (1), 237−243.
(22) Wilson, N. M.; Flaherty, D. W. Mechanism for the Direct Synthesis of H_2O_2 on Pd Clusters: Heterolytic Reaction Pathways at the Liquid−solid Interface. *J. Am. Chem. Soc.* **2016**, *138* (2), 574−586.
(23) Lim, E. J.; Kim, Y.; Choi, S. M.; Lee, S.; Noh, Y.; Kim, W. B. Binary PdM catalysts (M = Ru, Sn, or Ir) over a Reduced Graphene Oxide Support for Electro oxidation of Primary Alcohols (Methanol, Ethanol, 1 Propanol) under Alkaline Conditions. *J. Mater. Chem. A* **2015**, *3* (10), 5491−5500.
(24) Han, Y. F.; Lunsford, J. H. Direct Formation of H_2O_2 from H_2 and O_2 over a Pd/SiO_2 Catalyst: The Roles of the Acid and the Liquid Phase. *J. Catal.* **2005**, *230* (2), 313−316.
(25) Gallina, G.; García Serna, J.; Salmi, T. O.; Canu, P.; Biasi, P. Bromide and Acids: A Comprehensive Study on Their Role on the Hydrogen Peroxide Direct Synthesis. *Ind. Eng. Chem. Res.* **2017**, *56* (45), 13367−13378.
(26) Wilson, N. M.; Flaherty, D. W. Mechanism for the Direct Synthesis of H_2O_2 on Pd Clusters: Heterolytic Reaction Pathways at the Liquid−Solid Interface. *J. Am. Chem. Soc.* **2016**, *138* (2), 574−586.
(27) Tian, P.; Ouyang, L.; Xu, X.; Ao, C.; Xu, X.; Si, R.; Shen, X.; Lin, M.; Xu, J.; Han, Y. F. The Origin of Palladium Particle Size Effects in the Direct Synthesis of H_2O_2: Is Smaller Better? *J. Catal.* **2017**, *349*, 30−40.
(28) Jeong, H. E.; Kim, S.; Seo, M. G.; Lee, D. W.; Lee, K. Y. Catalytic activity of Pd octahedrons/SiO_2 for the direct synthesis of hydrogen peroxide from hydrogen and oxygen. *J. Mol. Catal. A: Chem.* **2016**, *420*, 88−95.
(29) Kim, S.; Lee, D. W.; Lee, K. Y. Direct Synthesis of Hydrogen Peroxide from Hydrogen and Oxygen over Single crystal Cubic Palladium on Silica Catalysts. *J. Mol. Catal. A: Chem.* **2014**, *383−384*, 64−69.
(30) Seo, M. g.; Kim, H. J.; Han, S. S.; Lee, K. Y. Direct Synthesis of Hydrogen Peroxide from Hydrogen and Oxygen Using Tailored Pd Nanocatalysts: A Review of Recent Findings. *Catal. Surv. Asia* **2017**, *21* (1), 1−12.
(31) Lari, G. M.; Puértolas, B.; Shahrokhi, M.; López, N.; Pérez Ramírez, J. Hybrid Palladium Nanoparticles for Direct Hydrogen Peroxide Synthesis: The Key Role of the Ligand. *Angew. Chem.* **2017**, *129*, 1801−1805.
(32) Edwards, J. K.; Solsona, B.; N, E. N.; Carley, A. F.; Herzing, A. A.; Kiely, C. J.; Hutchings, G. J. Switching Off Hydrogen Peroxide Hydrogenation in the Direct Synthesis Process. *Science* **2009**, *323* (5917), 1037−1041.
(33) Ntainjua N., E.; Edwards, J. K.; Carley, A. F.; Lopez Sanchez, J. A.; Moulijn, J. A.; Herzing, A. A.; Kiely, C. J.; Hutchings, G. J. The Role of the Support in Achieving High Selectivity in the Direct Formation of Hydrogen Peroxide. *Green Chem.* **2008**, *10* (11), 1162−1169.
(34) Lewis, R. J.; Edwards, J. K.; Freakley, S. J.; Hutchings, G. J. Solid Acid Additives as Recoverable Promoters for the Direct Synthesis of Hydrogen Peroxide. *Ind. Eng. Chem. Res.* **2017**, *56* (45), 13287−13293.
(35) Edwards, J. K.; Freakley, S. J.; Carley, A. F.; Kiely, C. J.; Hutchings, G. J. Strategies for Designing Supported Gold Palladium Bimetallic Catalysts for the Direct Synthesis of Hydrogen Peroxide. *Acc. Chem. Res.* **2014**, *47* (3), 845−54.
(36) Wilson, N. M.; Pan, Y. T.; Shao, Y. T.; Zuo, J. M.; Yang, H.; Flaherty, D. W. Direct Synthesis of H_2O_2 on AgPt Octahedra: The Importance of Ag−Pt Coordination for High H_2O_2 Selectivity. *ACS Catal.* **2018**, *8* (4), 2880−2889.
(37) Wang, S.; Lewis, R. J.; Doronkin, D. E.; Morgan, D. J.; Grunwaldt, J. D.; Hutchings, G. J.; Behrens, S. The Direct Synthesis of Hydrogen Peroxide from H_2 and O_2 Using Pd Ga and Pd In Catalysts. *Catal. Sci. Technol.* **2020**, *10*, 1925−1932.
(38) Wang, S.; Doronkin, D. E.; Hähsler, M.; Huang, X.; Wang, D.; Grunwaldt, J. D.; Behrens, S. Palladium Based Bimetallic Nanocrystal Catalysts for the Direct Synthesis of Hydrogen Peroxide. *Chem SusChem* **2020**, *13*, 3243−3251.
(39) Freakley, S. J.; He, Q.; Harrhy, J. H.; Lu, L.; Crole, D. A.; Morgan, D. J.; Ntainjua, E. N.; Edwards, J. K.; Carley, A. F.; Borisevich, A. Y. Palladium Tin Catalysts for the Direct Synthesis of H_2O_2 with High Selectivity. *Science* **2016**, *351* (6276), 965−968.
(40) Ding, D.; Xu, X.; Tian, P.; Liu, X.; Xu, J.; Han, Y. F. Promotional Effects of Sb on Pd based Catalysts for the Direct Synthesis of Hydrogen Peroxide at Ambient Pressure. *Chinese Journal of Catalysis* **2018**, *39* (4), 673−681.

(41) Tian, P.; Xu, X.; Ao, C.; Ding, D.; Li, W.; Si, R.; Tu, W.; Xu, J.; Han, Y. F. Direct and Selective Synthesis of Hydrogen Peroxide over Palladium Tellurium Catalysts at Ambient Pressure. *ChemSusChem* **2017**, *10* (17), 3342−3346.
(42) Edwards, J. K.; Freakley, S. J.; Carley, A. F.; Kiely, C. J.; Hutchings, G. J. Strategies for Designing Supported Gold−Palladium Bimetallic Catalysts for the Direct Synthesis of Hydrogen Peroxide. *Acc. Chem. Res.* **2014**, *47*, 845.
(43) Wilson, N. M.; Priyadarshini, P.; Kunz, S.; Flaherty, D. W. Direct Synthesis of H_2O_2 on Pd and Au_xPd_1 Clusters: Understanding the Effects of Alloying Pd with Au. *J. Catal.* **2018**, *357*, 163−175.
(44) Li, F.; Shao, Q.; Hu, M.; Chen, Y.; Huang, X. Hollow Pd−Sn Nanocrystals for Efficient Direct H_2O_2 Synthesis: The Critical Role of Sn on Structure Evolution and Catalytic Performance. *ACS Catal.* **2018**, *8*, 3418−3423.
(45) Ham, H. C.; Stephens, J. A.; Hwang, G. S.; Han, J.; Nam, S. W.; Lim, T. H. Pd Ensemble Effects on Oxygen Hydrogenation in AuPd Alloys: A Combined Density Functional Theory and Monte Carlo Study. *Catal. Today* **2011**, *165* (1), 138−144.
(46) Ledendecker, M.; Pizzutilo, E.; Malta, G.; Fortunato, G. V.; Mayrhofer, K. J. J.; Hutchings, G. J.; Freakley, S. J. Isolated Pd Sites as Selective Catalysts for Electrochemical and Direct Hydrogen Peroxide Synthesis. *ACS Catal.* **2020**, *10* (10), 5928−5938.
(47) Han, G. H.; Xiao, X.; Hong, J.; Lee, K. J.; Park, S.; Ahn, J. P.; Lee, K. Y.; Yu, T. Tailored Palladium−Platinum Nanoconcave Cubes as High Performance Catalysts for the Direct Synthesis of Hydrogen Peroxide. *ACS Appl. Mater. Interfaces* **2020**, *12* (5), 6328−6335.
(48) Strasser, P.; Koh, S.; Anniyev, T.; Greeley, J.; More, K.; Yu, C.; Liu, Z.; Kaya, S.; Nordlund, D.; Ogasawara, H.; Toney, M. F.; Nilsson, A. Lattice strain Control of the Activity in Dealloyed Core shell Fuel Cell Catalysts. *Nat. Chem.* **2010**, *2* (6), 454−60.
(49) Grabow, L. C.; Hvolbæk, B.; Falsig, H.; Nørskov, J. K. Search Directions for Direct H_2O_2 Synthesis Catalysts Starting from Au_{12} Nanoclusters. *Top. Catal.* **2012**, *55* (5−6), 336−344.
(50) Xu, H.; Cheng, D.; Gao, Y. Design of High Performance Pd Based Alloy Nanocatalysts for Direct Synthesis of H_2O_2. *ACS Catal.* **2017**, *7* (3), 2164−2170.
(51) Vilé, G.; Almora Barrios, N.; Mitchell, S.; López, N.; Pérez Ramírez, J. From the Lindlar Catalyst to Supported Ligand Modified Palladium Nanoparticles: Selectivity Patterns and Accessibility Constraints in the Continuous Flow Three Phase Hydrogenation of Acetylenic Compounds. *Chem. Eur. J.* **2014**, *20* (20), 5849−5849.
(52) Edwards, J. K.; Solsona, B.; N, E. N.; Carley, A. F.; Herzing, A. A.; Kiely, C. J.; Hutchings, G. J. Switching off Hydrogen Peroxide Hydrogenation in the Direct Synthesis Process. *Science* **2009**, *323* (5917), 1037−41.
(53) Wang, Y.; Wöll, C. IR Spectroscopic Investigations of Chemical and Photochemical Reactions on Metal Oxides: Bridging the Materials Gap. *Chem. Soc. Rev.* **2017**, *46* (7), 1875−1932.
(54) Cheng, J.; Wang, C.; Zhang, S. Methods to Determine the Mine Gas Explosibility − An overview. *J. Loss Prev. Process Ind.* **2012**, *25* (3), 425−435.
(55) Liu, Q.; Lunsford, J. H. Controlling Factors in the Direct Formation of H_2O_2 from H_2 and O_2 over a Pd/SiO_2 Catalyst in Ethanol. *Appl. Catal., A* **2006**, *314* (1), 94−100.
(56) Kresse, G.; Hafner, J. Ab initio Molecular Dynamics for Liquid Metals. *Phys. Rev. B: Condens. Matter Mater. Phys.* **1993**, *47* (1), 558−561.
(57) Kresse, G.; Hafner, J. Ab initio Molecular Dynamics Simulation of the Liquid Metal Amorphous Semiconductor Transition in Ger manium. *Phys. Rev. B: Condens. Matter Mater. Phys.* **1994**, *49* (20), 14251−14269.
(58) Kresse, G.; Furthmüller, J. Efficient Iterative Schemes for ab initio Total energy Calculations Using a Plane wave Basis Set. *Phys. Rev. B: Condens. Matter Mater. Phys.* **1996**, *54* (16), 11169−11186.
(59) Kresse, G.; Furthmüller, J. Efficiency of ab initio Total Energy Calculations for Metals and Semiconductors Using a Plane wave Basis Set. *Comput. Mater. Sci.* **1996**, *6* (1), 15−50.
(60) Mortensen, J. J.; Kaasbjerg, K.; Frederiksen, S. L.; Nørskov, J. K.; Sethna, J. P.; Jacobsen, K. W. Bayesian Error Estimation in Density Functional Theory. *Phys. Rev. Lett.* **2005**, *95* (21), 216401.
(61) Wellendorff, J.; Lundgaard, K. T.; Møgelhøj, A.; Petzold, V.; Landis, D. D.; Nørskov, J. K.; Bligaard, T.; Jacobsen, K. W. Density Functionals for Surface Science: Exchange correlation Model Development with Bayesian Error Estimation. *Phys. Rev. B: Condens. Matter Mater. Phys.* **2012**, *85* (23), 235149.
(62) Blöchl, P. E. Projector Augmented wave Method. *Phys. Rev. B: Condens. Matter Mater. Phys.* **1994**, *50* (24), 17953−17979.
(63) Kresse, G.; Joubert, D. From Ultrasoft Pseudopotentials to the Projector Augmented wave Method. *Phys. Rev. B: Condens. Matter Mater. Phys.* **1999**, *59* (3), 1758−1775.
(64) Mallikarjun Sharada, S.; Bligaard, T.; Luntz, A. C.; Kroes, G. J.; Nørskov, J. K. SBH10: A Benchmark Database of Barrier Heights on Transition Metal Surfaces. *J. Phys. Chem. C* **2017**, *121* (36), 19807−19815.
(65) Wellendorff, J.; Silbaugh, T. L.; Garcia Pintos, D.; Nørskov, J. K.; Bligaard, T.; Studt, F.; Campbell, C. T. A Benchmark Database for Adsorption Bond Energies to Transition Metal Surfaces and Comparison to Selected DFT Functionals. *Surf. Sci.* **2015**, *640*, 36−44.
(66) Duanmu, K.; Truhlar, D. G. Validation of Density Functionals for Adsorption Energies on Transition Metal Surfaces. *J. Chem. Theory Comput.* **2017**, *13* (2), 835−842.
(67) Cargnello, M.; Doan Nguyen, V. V. T.; Murray, C. B. Engineering Uniform Nanocrystals: Mechanism of Formation and Self assembly into Bimetallic Nanocrystal Superlattices. *AIChE J.* **2016**, *62* (2), 392−398.
(68) Cargnello, M.; Doan Nguyen, V. V. T.; Gordon, T. R.; Diaz, R. E.; Stach, E. A.; Gorte, R. J.; Fornasiero, P.; Murray, C. B. Control of Metal Nanocrystal Size Reveals Metal Support Interface Role for Ceria Catalysts. *Science* **2013**, *341* (6147), 771−773.
(69) Kim, S. W.; Park, J.; Jang, Y.; Chung, Y.; Hwang, S.; Hyeon, T.; Kim, Y. W. Synthesis of Monodisperse Palladium Nanoparticles. *Nano Lett.* **2003**, *3* (9), 1289−1291.
(70) Kwon, S. G.; Hyeon, T. Colloidal Chemical Synthesis and Formation Kinetics of Uniformly Sized Nanocrystals of Metals, Oxides, and Chalcogenides. *Acc. Chem. Res.* **2008**, *41* (12), 1696−1709.
(71) Amatore, C.; Jutand, A.; M'Barki, M. A. Evidence of the Formation of Zerovalent Palladium from $Pd(OAc)_2$ and Triphenyl phosphine. *Organometallics* **1992**, *11* (9), 3009−3013.
(72) Kang, Y.; Pyo, J. B.; Ye, X.; Gordon, T. R.; Murray, C. B. Synthesis, Shape Control, and Methanol Electro oxidation Properties of Pt−Zn Alloy and Pt_3Zn Intermetallic Nanocrystals. *ACS Nano* **2012**, *6* (6), 5642−5647.
(73) Willis, J. J.; Goodman, E. D.; Wu, L.; Riscoe, A. R.; Martins, P.; Tassone, C. J.; Cargnello, M. Systematic Identification of Promoters for Methane Oxidation Catalysts Using Size and Composition Controlled Pd Based Bimetallic Nanocrystals. *J. Am. Chem. Soc.* **2017**, *139* (34), 11989−11997.
(74) Chen, T.; Rodionov, V. O. Controllable Catalysis with Nanoparticles: Bimetallic Alloy Systems and Surface Adsorbates. *ACS Catal.* **2016**, *6* (6), 4025−4033.
(75) F. de L. e Freitas, L.; Puértolas, B.; Zhang, J.; Wang, B.; Hoffman, A. S.; Bare, S. R.; Pérez Ramírez, J.; Medlin, J. W.; Nikolla, E. Tunable Catalytic Performance of Palladium Nanoparticles for H_2O_2 Direct Synthesis via Surface Bound Ligands. *ACS Catal.* **2020**, *10* (9), 5202−5207.
(76) Tian, P.; Xu, X.; Ao, C.; Ding, D.; Li, W.; Si, R.; Tu, W.; Xu, J.; Han, Y. F. Direct and Selective Synthesis of Hydrogen Peroxide over Palladium−Tellurium Catalysts at Ambient Pressure. *ChemSusChem* **2017**, *10* (17), 3342−3346.
(77) Santos, A.; Lewis, R. J.; Malta, G.; Howe, A. G. R.; Morgan, D. J.; Hampton, E.; Gaskin, P.; Hutchings, G. J. Direct Synthesis of Hydrogen Peroxide over Au−Pd Supported Nanoparticles under Ambient Conditions. *Ind. Eng. Chem. Res.* **2019**, *58* (28), 12623−12631.

(78) Freakley, S. J.; He, Q.; Harrhy, J. H.; Lu, L.; Crole, D. A.; Morgan, D. J.; Ntainjua, E. N.; Edwards, J. K.; Carley, A. F.; Borisevich, A. Y.; Kiely, C. J.; Hutchings, G. J. Palladium Tin catalysts for the Direct Synthesis of H_2O_2 with High Selectivity. *Science* **2016**, *351* (6276), 965–968.
(79) Solsona, B. E.; Edwards, J. K.; Landon, P.; Carley, A. F.; Herzing, A.; Kiely, C. J.; Hutchings, G. J. Direct Synthesis of Hydrogen Peroxide from H_2 and O_2 Using Al_2O_3 Supported Au– Pd Catalysts. *Chem. Mater.* **2006**, *18* (11), 2689–2695.
(80) Han, Y. F.; Zhong, Z.; Ramesh, K.; Chen, F.; Chen, L.; White, T.; Tay, Q.; Yaakub, S. N.; Wang, Z. Au Promotional Effects on the Synthesis of H_2O_2 Directly from H_2 and O_2 on Supported Pd–Au Alloy Catalysts. *J. Phys. Chem. C* **2007**, *111* (24), 8410–8413.
(81) Wilson, N. M.; Schröder, J.; Priyadarshini, P.; Bregante, D. T.; Kunz, S.; Flaherty, D. W. Direct Synthesis of H_2O_2 on PdZn Nanoparticles: The Impact of Electronic Modifications and Heterogeneity of Active Sites. *J. Catal.* **2018**, *368*, 261–274.
(82) Bernardotto, G.; Menegazzo, F.; Pinna, F.; Signoretto, M.; Cruciani, G.; Strukul, G. New Pd–Pt and Pd–Au Catalysts for an Efficient Synthesis of H_2O_2 from H_2 and O_2 under very Mild Conditions. *Appl. Catal., A* **2009**, *358* (2), 129–135.
(83) Li, G.; Edwards, J.; Carley, A. F.; Hutchings, G. J. Direct Synthesis of Hydrogen Peroxide from H_2 and O_2 Using Zeolite Supported Au Catalysts. *Catal. Today* **2006**, *114* (4), 369–371.
(84) Alotaibi, F.; Al Mayman, S.; Alotaibi, M.; Edwards, J. K.; Lewis, R. J.; Alotaibi, R.; Hutchings, G. J. Direct Synthesis of Hydrogen Peroxide Using Cs Containing Heteropolyacid Supported Palladi um–Copper Catalysts. *Catal. Lett.* **2019**, *149* (4), 998–1006.
(85) Lee, S.; Chung, Y. M. An Efficient Pd/C Catalyst Design Based on SequentialLigand Exchange Method for the Direct Synthesis of H_2O_2. *Mater. Lett.* **2019**, *234*, 58–61.
(86) Edwards, J. K.; Freakley, S. J.; Lewis, R. J.; Pritchard, J. C.; Hutchings, G. J. Advances in the Direct Synthesis of Hydrogen Peroxide from Hydrogen and Oxygen. *Catal. Today* **2015**, *248*, 3–9.
(87) Park, S.; Lee, J.; Song, J. H.; Kim, T. J.; Chung, Y. M.; Oh, S. H.; Song, I. K. Direct Synthesis of Hydrogen Peroxide from Hydrogen and Oxygen over Pd/HZSM 5 catalysts: Effect of Brönsted Acidity. *J. Mol. Catal. A: Chem.* **2012**, *363–364*, 230–236.
(88) Ropero Vega, J. L.; Aldana Pérez, A.; Gómez, R.; Niño Gómez, M. E. Sulfated Titania [TiO_2/SO_4^{2-}]: A very Active Solid Acid Catalyst for the Esterification of Free Fatty Acids with Ethanol. *Appl. Catal., A* **2010**, *379* (1), 24–29.
(89) Chen, A.; Yu, X.; Zhou, Y.; Miao, S.; Li, Y.; Kuld, S.; Sehested, J.; Liu, J.; Aoki, T.; Hong, S.; Camellone, M. F.; Fabris, S.; Ning, J.; Jin, C.; Yang, C.; Nefedov, A.; Wöll, C.; Wang, Y.; Shen, W. Structure of the Catalytically Active Copper–Ceria Interfacial Perimeter. *Nature Catalysis* **2019**, *2* (4), 334–341.
(90) Wöll, C. Structure and Chemical Properties of Oxide Nanoparticles Determined by Surface Ligand IR Spectroscopy. *ACS Catal.* **2020**, *10* (1), 168–176.
(91) Tofighi, G.; Yu, X.; Lichtenberg, H.; Doronkin, D. E.; Wang, W.; Wöll, C.; Wang, Y.; Grunwaldt, J. D. Chemical Nature of Microfluidically Synthesized AuPd Nanoalloys Supported on TiO_2. *ACS Catal.* **2019**, *9* (6), 5462–5473.
(92) Kolb, D. M.; Przasnyski, M.; Gerischer, H. Underpotential Deposition of Metals and Work Function Differences. *J. Electroanal. Chem. Interfacial Electrochem.* **1974**, *54* (1), 25–38.
(93) Freakley, S. J.; Piccinini, M.; Edwards, J. K.; Ntainjua, E. N.; Moulijn, J. A.; Hutchings, G. J. Effect of Reaction Conditions on the Direct Synthesis of Hydrogen Peroxide with a AuPd/TiO_2 Catalyst in a Flow Reactor. *ACS Catal.* **2013**, *3* (4), 487–501.
(94) Furukawa, S.; Komatsu, T. Intermetallic Compounds: Promising Inorganic Materials for Well Structured and Electronically Modified Reaction Environments for Efficient Catalysis. *ACS Catal.* **2017**, *7* (1), 735–765.
(95) Yan, Y.; Du, J. S.; Gilroy, K. D.; Yang, D.; Xia, Y.; Zhang, H. Intermetallic Nanocrystals: Syntheses and Catalytic Applications. *Adv. Mater.* **2017**, *29* (14), 1605997.
(96) Bu, L.; Shao, Q.; Pi, Y.; Yao, J.; Luo, M.; Lang, J.; Hwang, S.; Xin, H.; Huang, B.; Guo, J.; Su, D.; Guo, S.; Huang, X. Coupled s p d Exchange in Facet Controlled Pd_3Pb Tripods Enhances Oxygen Reduction Catalysis. *Chem.* **2018**, *4* (2), 359–371.
(97) Mostafa, S.; Behafarid, F.; Croy, J. R.; Ono, L. K.; Li, L.; Yang, J. C.; Frenkel, A. I.; Cuenya, B. R. Shape Dependent Catalytic Properties of Pt Nanoparticles. *J. Am. Chem. Soc.* **2010**, *132* (44), 15714–15719.
(98) Kim, S.; Lee, D. W.; Lee, K. Y. Shape Dependent Catalytic Activity of Palladium Nanoparticles for the Direct Synthesis of Hydrogen Peroxide from Hydrogen and Oxygen. *J. Mol. Catal. A: Chem.* **2014**, *391*, 48–54.
(99) Han, G. H.; Kim, K. Y.; Nam, H.; Kim, H.; Yoon, J.; Lee, J. H.; Kim, H. K.; Ahn, J. P.; Lee, S. Y.; Lee, K. Y.; Yu, T. Facile Direct Seed Mediated Growth of AuPt Bimetallic Shell on the Surface of Pd Nanocubes and Application for Direct H_2O_2 Synthesis. *Catalysts* **2020**, *10* (6), 650.
(100) Doronkin, D. E.; Wang, S.; Sharapa, D. I.; Deschner, B. J.; Sheppard, T. L.; Zimina, A.; Studt, F.; Dittmeyer, R.; Behrens, S.; Grunwaldt, J. D. Dynamic Structural Changes of Supported Pd, PdSn, and PdIn Nanoparticles during Continuous Flow High Pressure Direct H_2O_2 Synthesis. *Catal. Sci. Technol.* **2020**, *10* (14), 4726–4742.
(101) Plauck, A.; Stangland, E. E.; Dumesic, J. A.; Mavrikakis, M. Active Sites and Mechanisms for H_2O_2 Decomposition over Pd Catalysts. *Proc. Natl. Acad. Sci. U. S. A.* **2016**, *113* (14), E1973–E1982.
(102) Oğuz, I. C.; Mineva, T.; Guesmi, H. The Effect of Pd Ensemble Structure on the O_2 Dissociation and CO Oxidation Mechanisms on Au—Pd(100) Surface Alloys. *J. Chem. Phys.* **2018**, *148* (2), 024701.
(103) Cheng, F.; Chen, J. Metal–Air Batteries: From Oxygen Reduction Electrochemistry to Cathode Catalysts. *Chem. Soc. Rev.* **2012**, *41* (6), 2172–2192.
(104) Zinola, C. F.; Arvia, A. J.; Estiu, G. L.; Castro, E. A. A Quantum Chemical Approach to the Influence of Platinum Surface Structure on the Oxygen Electroreduction Reaction. *J. Phys. Chem.* **1994**, *98* (31), 7566–7576.
(105) Duan, Z.; Wang, G. Comparison of Reaction Energetics for Oxygen Reduction Reactions on Pt(100), Pt(111), Pt/Ni(100), and Pt/Ni(111) Surfaces: A First Principles Study. *J. Phys. Chem. C* **2013**, *117* (12), 6284–6292.
(106) Li, K.; Li, Y.; Wang, Y.; He, F.; Jiao, M.; Tang, H.; Wu, Z. The Oxygen Reduction Reaction on Pt(111) and Pt(100) Surfaces Substituted by Subsurface Cu: A Theoretical Perspective. *J. Mater. Chem. A* **2015**, *3* (21), 11444–11452.
(107) Behtash, S.; Lu, J.; Mamun, O.; Williams, C. T.; Monnier, J. R.; Heyden, A. Solvation Effects in the Hydrodeoxygenation of Propanoic Acid over a Model Pd(211) Catalyst. *J. Phys. Chem. C* **2016**, *120* (5), 2724–2736.
(108) Chen, J. S.; Yao, C.; Liu, X. J.; Zhang, X.; Sun, C. Q.; Huang, Y. L. H_2O_2 and HO– Solvation Dynamics: Solute Capabilities and Solute Solvent Molecular Interactions. *ChemistrySelect* **2017**, *2* (27), 8517–8523.
(109) Dissanayake, D. P.; Lunsford, J. H. The Direct Formation of H_2O_2 from H_2 and O_2 over Colloidal Palladium. *J. Catal.* **2003**, *214* (1), 113–120.